Supplementary Information

Full-course NIR-II imaging-navigated fractionated photodynamic therapy of bladder tumours with X-ray-activated nanotransducers

Liangrui He[1], Liyang Wang[2], Xujiang Yu[1], Yizhang Tang[1], Zhao Jiang[1], Guoliang Yang[2]*, Zhuang Liu[3]* and Wanwan Li[1]**

[1] State Key Lab of Metal Matrix Composites
School of Materials Science and Engineering
Zhangjiang Institute for Advanced Study
Shanghai Jiao Tong University
800 Dongchuan Road, Shanghai 200240, P. R. China

[2] Department of Urology, Renji Hospital
School of Medicine
Shanghai Jiao Tong University
1630 Dongfang Road, Shanghai 200127, P. R. China

[3] Institute of Functional Nano & Soft Materials (FUNSOM)
Soochow University
Suzhou, Jiangsu 215123, P. R. China

Table of Contents

Supplementary Figures

Supplementary Figure 1 4
Supplementary Figure 2 5
Supplementary Figure 3 6
Supplementary Figure 4 6
Supplementary Figure 5 7
Supplementary Figure 6 8
Supplementary Figure 7 8
Supplementary Figure 8 9
Supplementary Figure 9 10
Supplementary Figure 10 10
Supplementary Figure 11 11
Supplementary Figure 12 11
Supplementary Figure 13 11
Supplementary Figure 14 12
Supplementary Figure 15 13
Supplementary Figure 16 14
Supplementary Figure 17 14
Supplementary Figure 18 16
Supplementary Figure 19 16
Supplementary Figure 20 17
Supplementary Figure 21 17
Supplementary Figure 22 17
Supplementary Figure 23 18
Supplementary Figure 24 18
Supplementary Figure 25 19
Supplementary Figure 26 20
Supplementary Figure 27 21
Supplementary Figure 28 21
Supplementary Figure 29 21
Supplementary Figure 30 22
Supplementary Figure 31 22
Supplementary Figure 32 22
Supplementary Figure 33 23
Supplementary Figure 34 24
Supplementary Figure 35 24
Supplementary Figure 36 25
Supplementary Figure 37 25
Supplementary Figure 38 25
Supplementary Figure 39 26
Supplementary Figure 40 26

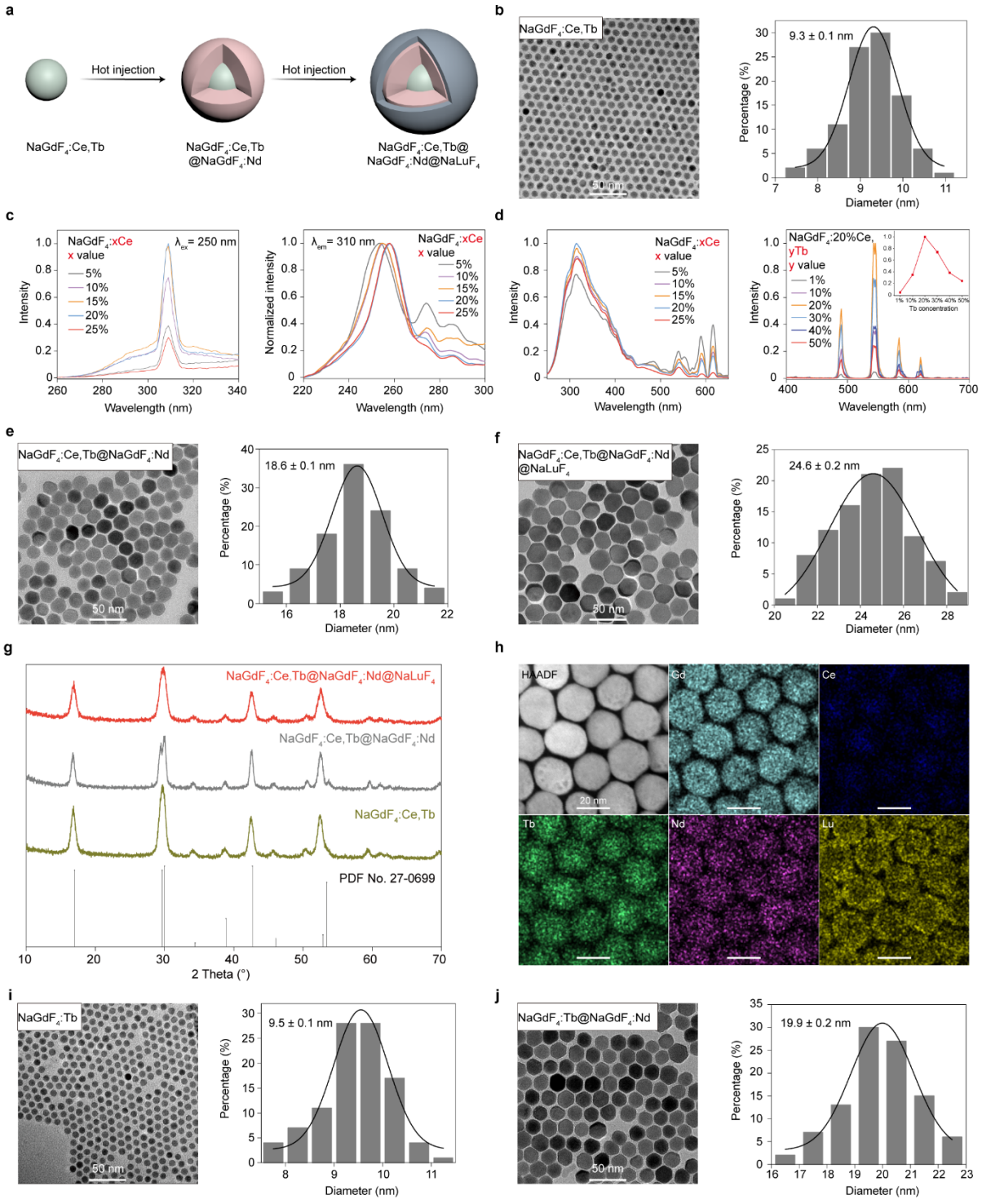
Supplementary Figure 41 27
Supplementary Figure 42 27

Table of Contents

Supplementary Tables

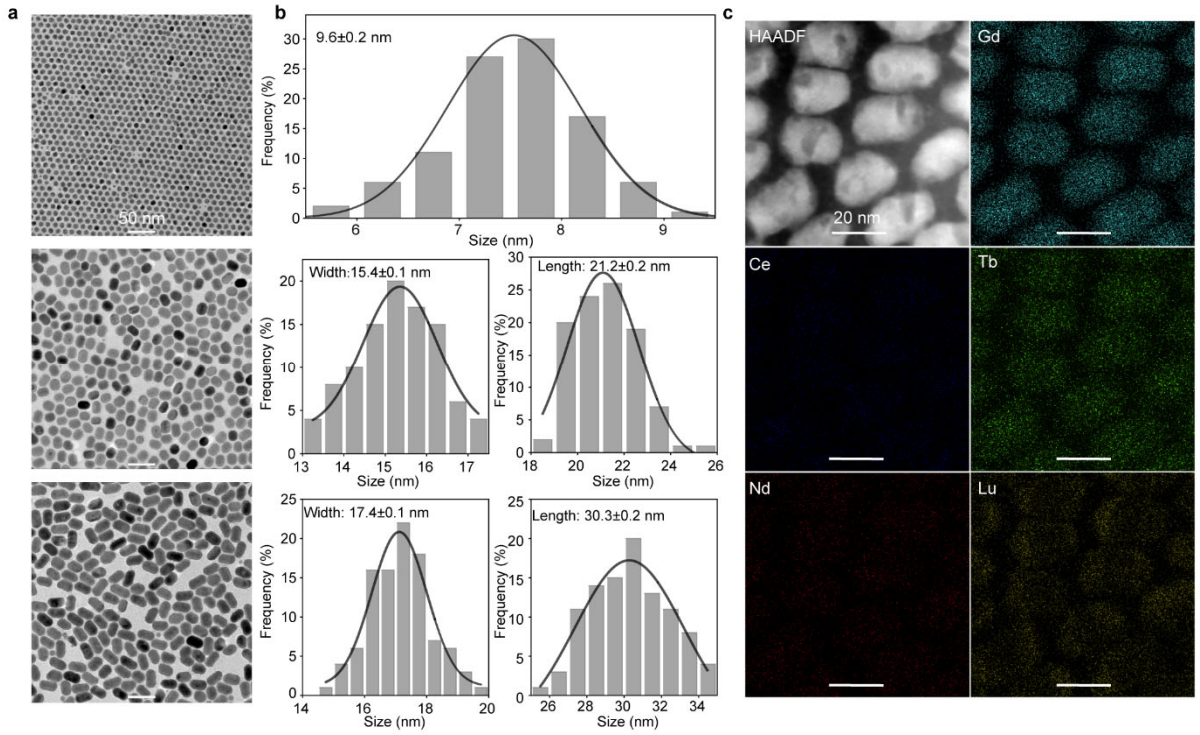
Supplementary Table 1 28
Supplementary Table 2 28
Supplementary Table 3 29

Supplementary Figures

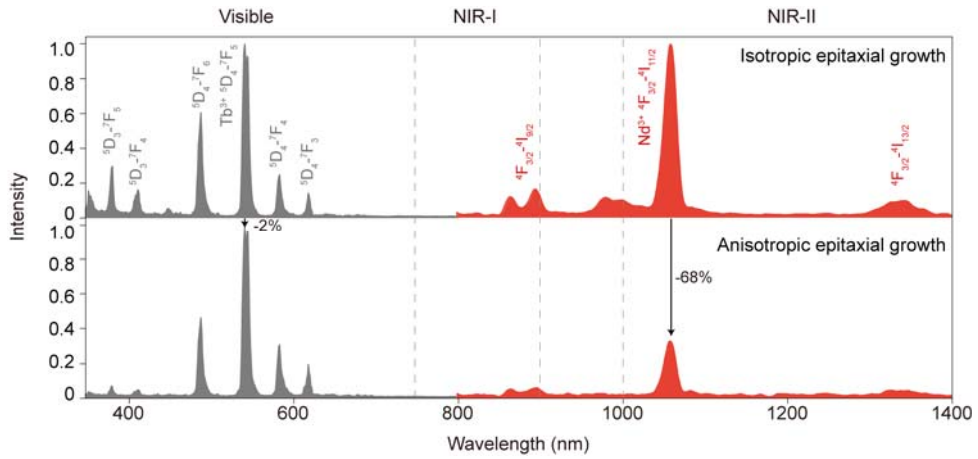


Supplementary Figure 1 | Nanoscintillator synthesis and characterization. a, Synthesis route of nanoscintillators. **b**, TEM image (left) and size distribution (right) of $NaGdF_4$:Ce,Tb. **c**, Photoluminescence emission spectra of $NaGdF_4$:xCe (ex: 250 nm) (left) and excitation spectra (right) of $NaGdF_4$:xCe (em: 310 nm). **d**, X-ray-activated spectra of $NaGdF_4$:xCe (left) and $NaGdF_4$:20%Ce,yTb (right). **e**, TEM image (left) and size distribution (right) of $NaGdF_4$:Ce,Tb@$NaGdF_4$:Nd. **f**, TEM image (left) and size

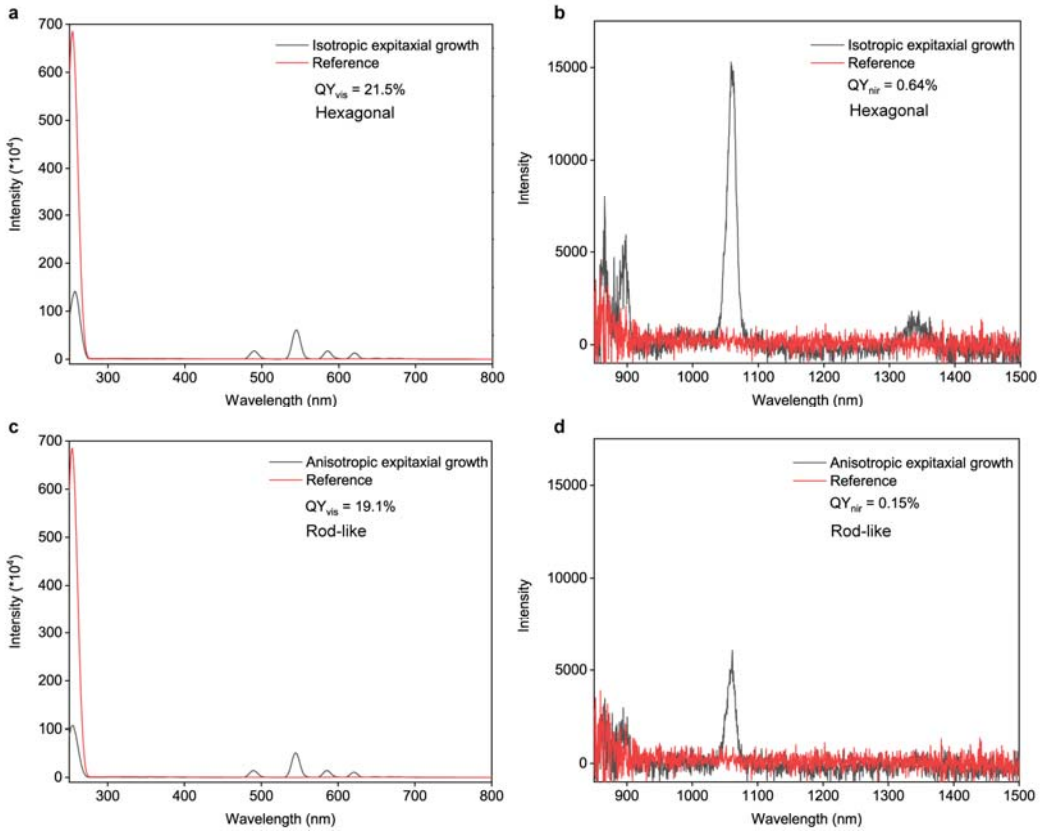
distribution (right) of $NaGdF_4$:Ce,Tb@$NaGdF_4$:Nd@$NaLuF_4$. **g**, X-ray diffraction (XRD) patterns of $NaGdF_4$:Ce,Tb, $NaGdF_4$:Ce,Tb@$NaGdF_4$:Nd, and $NaGdF_4$:Ce,Tb@$NaGdF_4$:Nd@$NaLuF_4$. **h**, High-angle annular dark-field (HAADF) and energy dispersive spectroscopy (EDS) of hexagonal $NaGdF_4$:Ce,Tb@$NaGdF_4$:Nd@$NaLuF_4$. **i**, TEM image (left) and size distribution (right) of $NaGdF_4$:Tb. **j**, TEM image (left) and size distribution (right) of $NaGdF_4$:Tb@$NaGdF_4$:Nd.



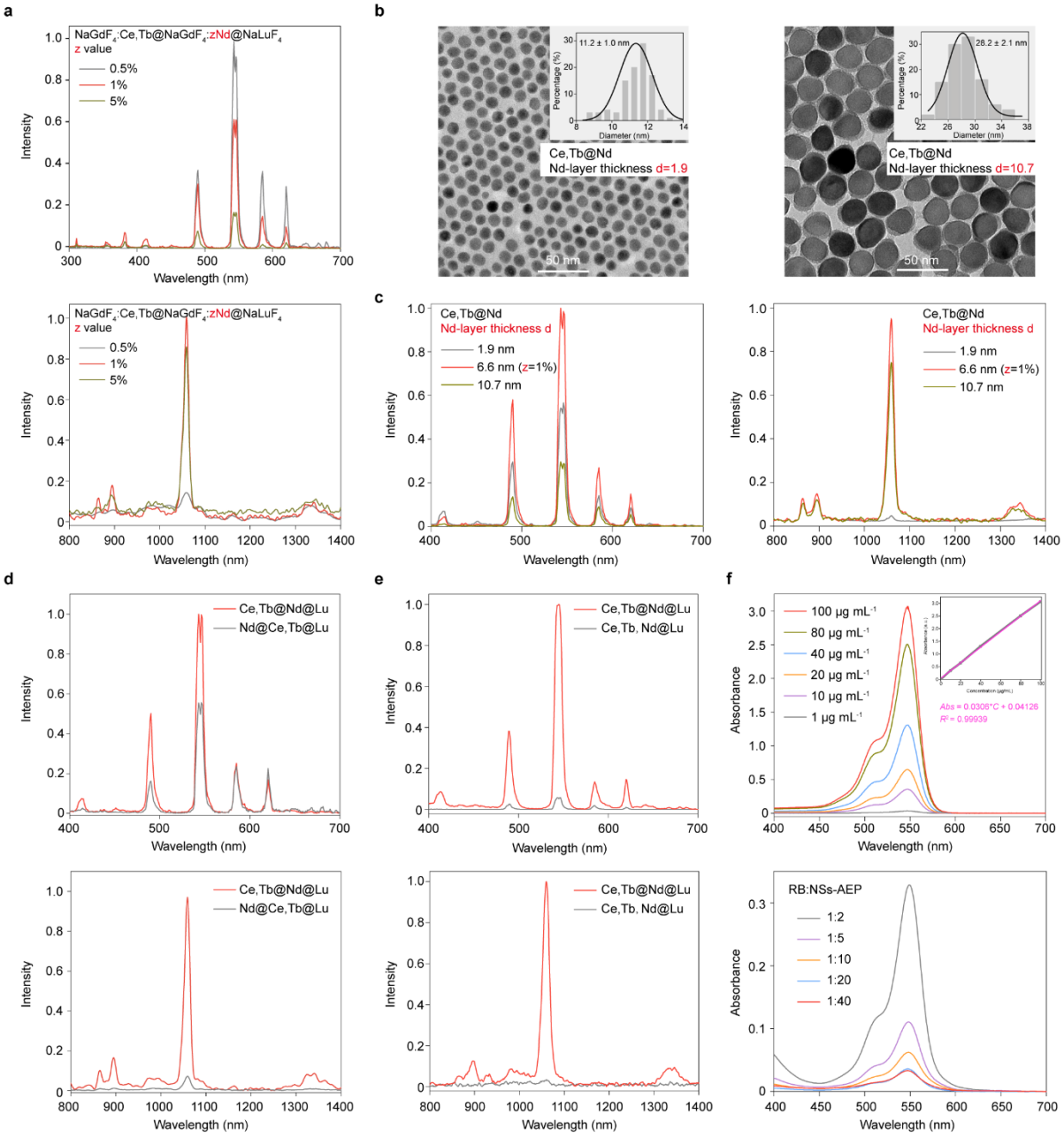
Supplementary Figure 2 | a, TEM images of $NaGdF_4$:Ce,Tb (top), rod-like $NaGdF_4$:Ce,Tb@$NaGdF_4$:Nd (medium), and rod-like $NaGdF_4$:Ce,Tb@$NaGdF_4$:Nd@$NaLuF_4$ (bottom) with anisotropic epitaxial growth. **b**, Size distribution of $NaGdF_4$:Ce,Tb (top), rod-like $NaGdF_4$:Ce,Tb@$NaGdF_4$:Nd (medium), and rod-like $NaGdF_4$:Ce,Tb@$NaGdF_4$:Nd@$NaLuF_4$ (bottom). **c**, High-angle annular dark-field (HAADF) and energy dispersive spectroscopy (EDS) of rod-like $NaGdF_4$:Ce,Tb@$NaGdF_4$:Nd@$NaLuF_4$.



Supplementary Figure 3 | Full spectra of hexganol $NaGdF_4$:Ce,Tb@$NaGdF_4$:Nd@$NaLuF_4$ with isotropic expitaxial growth (top) and rod-like $NaGdF_4$:Ce,Tb@$NaGdF_4$:Nd@$NaLuF_4$ with anisotropic expitaxial growth (bottom) under X-ray irradiation.

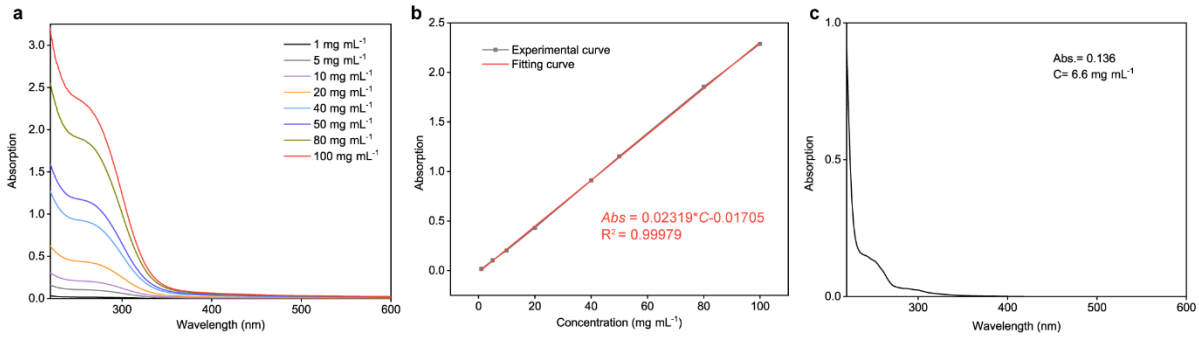


Supplementary Figure 4 | a,**b** Absolute fluorescence quantum yield of hexagonal $NaGdF_4$:Ce,Tb@$NaGdF_4$:Nd@$NaLuF_4$ with isotropic epitaxial growth in visible (**a**) and NIR-II spectra (**b**). **c**,**d** Absolute fluorescence quantum yield of rod-like $NaGdF_4$:Ce,Tb@$NaGdF_4$:Nd@$NaLuF_4$ with anisotropic epitaxial growth in visible (**c**) and NIR-II spectra (**d**).

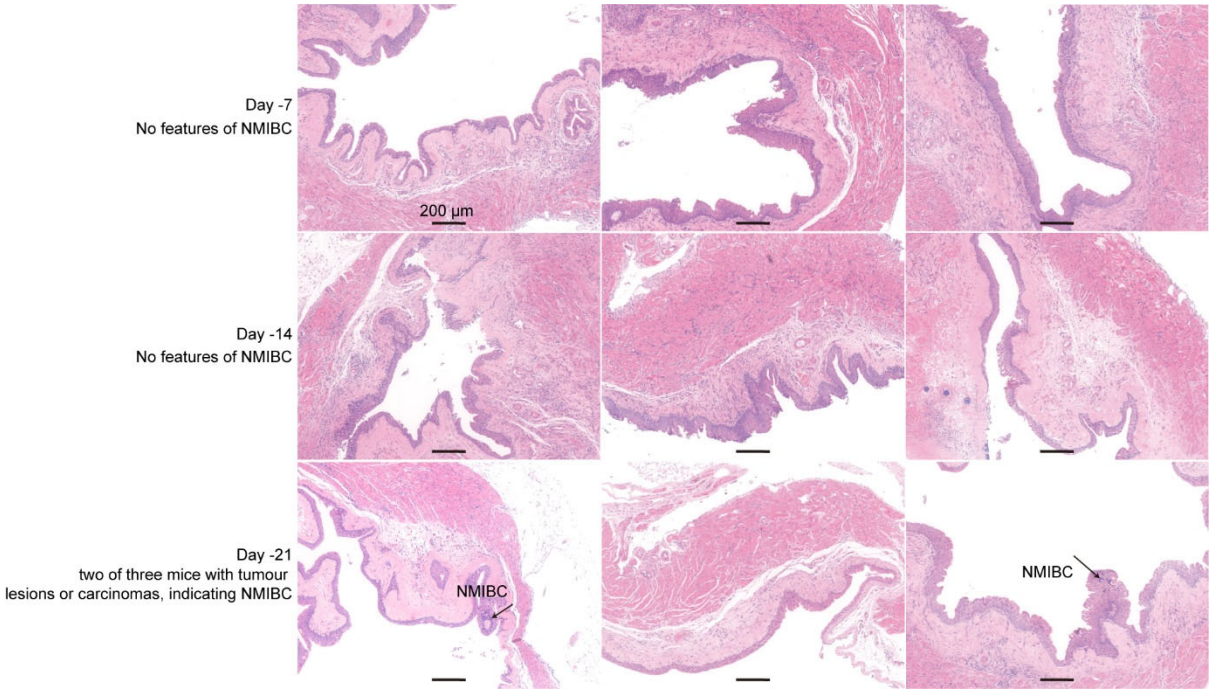


Supplementary Figure 5 | Optimization of X-ray-activated properties in nanoscintillators.a, X-ray-activated visible spectra (up) and NIR-II spectra (bottom) at different Nd doping concentrations. **b**, TEM images of $NaGdF_4$:Ce,Tb@$NaGdF_4$:Nd (denoted as Ce,Tb@Nd) with an Nd-layer thickness of 1.9 nm (left) and 10.7 nm (right). **c**, X-ray-activated visible spectra (left) and NIR-II spectra (right) of $NaGdF_4$:Ce,Tb@$NaGdF_4$:Nd (denoted as Ce,Tb@Nd) with corresponding Nd layers. **d**, X-ray-activated visible spectra (top) and NIR-II spectra (bottom) of $NaGdF_4$:Ce,Tb@$NaGdF_4$:Nd@$NaLuF_4$ (denoted as Ce,Tb@Nd@Lu) and $NaGdF_4$:Nd@$NaGdF_4$:Ce,Tb@$NaLuF_4$ (denoted as Nd@Ce,Tb@Lu) with the same doping ratios in each similar shell. **e**, X-ray-activated visible spectra (top) and NIR-II spectra (bottom) of $NaGdF_4$:Ce,Tb,Nd@$NaLuF_4$ (denoted as Ce,Tb,Nd@Lu). **f**, Absorption spectra of RB at various concentrations (top, insert is the linear fitting of

RB absorbance at 547 nm versus concentration) and supernatants after conjugation with different ratios of RB and NSs-AEP (bottom).

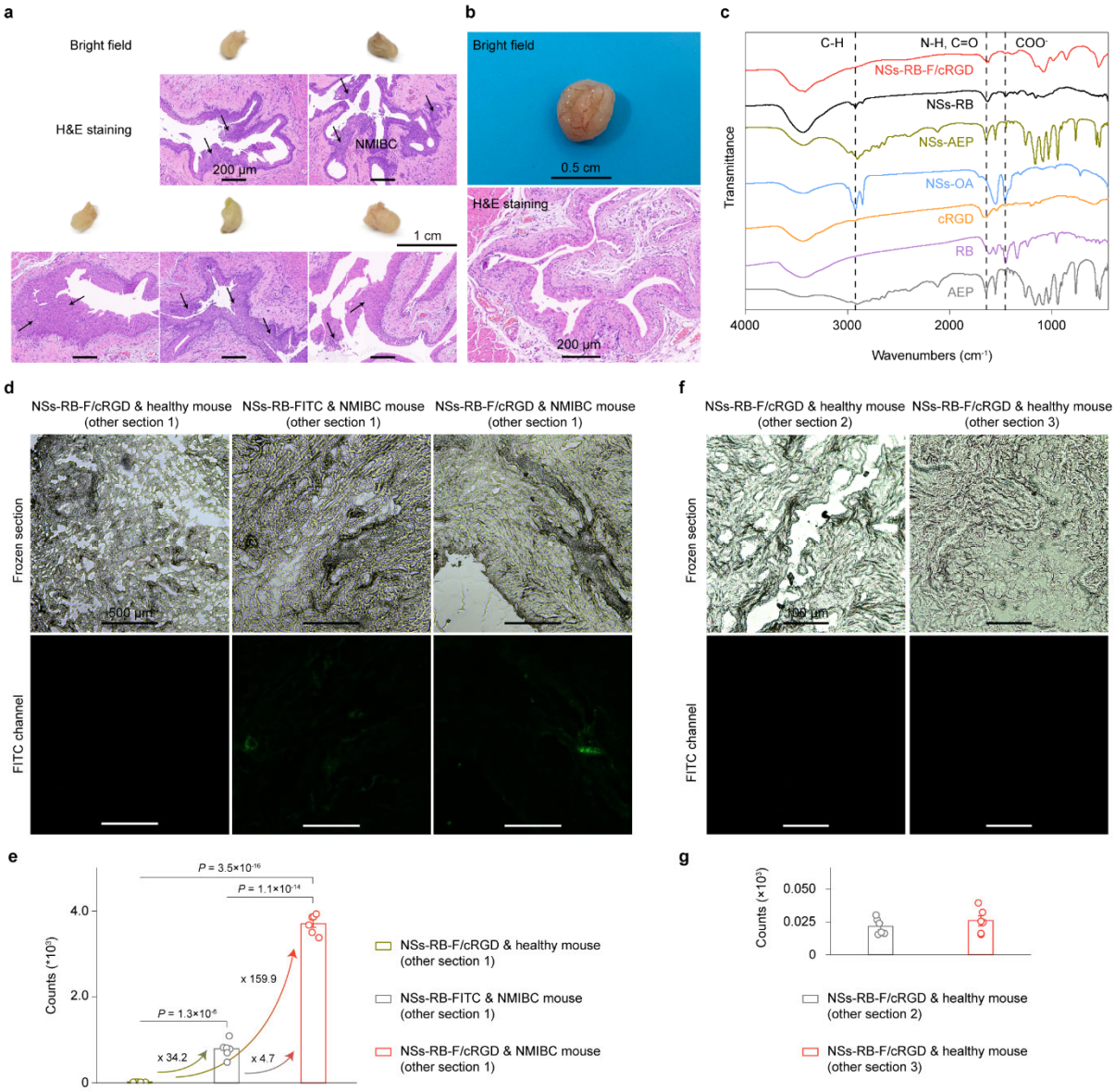


Supplementary Figure 6 | a, Absorption spectra of AEP at various concentrations. **b**, The linear fitting of AEP absorbance at 261 nm versus concentration. **c**, Absorption spectra of the supernatant of NSs after conjugation with AEP. Particularly, with the feeding amount of NSs to be 100 mg and the amount of AEP to be 750 mg, the concentration of the supernatant was measured to be 6.6 mg·mL^{-1} according to the standard curve with the volume parameter of the supernatant (50 mL). Therefore, the quantity of AEP in the supernatant was 330 mg, thus the mass ratio of AEP onto NSs could be calculated to be (750-330) mg:100 mg = 4.2:1.



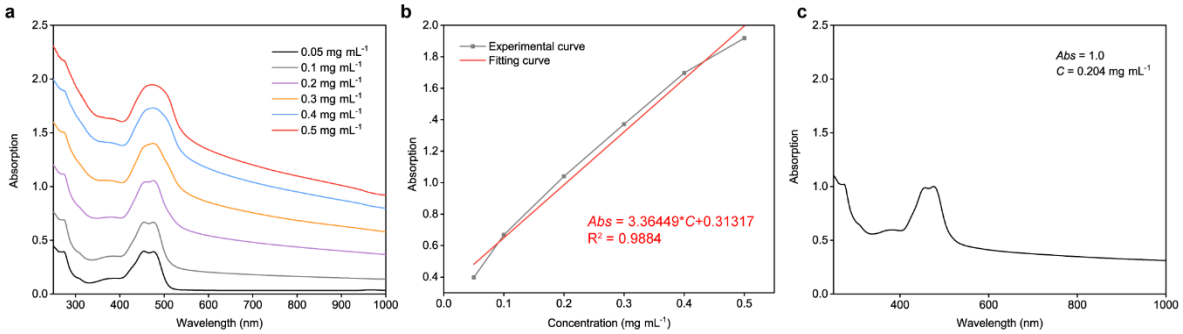
Supplementary Figure 7 | H&E staining results (n = 3 mice) of bladder from mice that received the fourth MNU instillation (namely day -28 as shown in Figure 5) for 7 days (marked as day -21 according to Figure 5a), 14 days (marked as day -14), and 21 days (marked as day -7), which indicated that at day -7, two of the three randomly selected mice were detected with apparent appearance of tumour carcinomas in the

bladder.

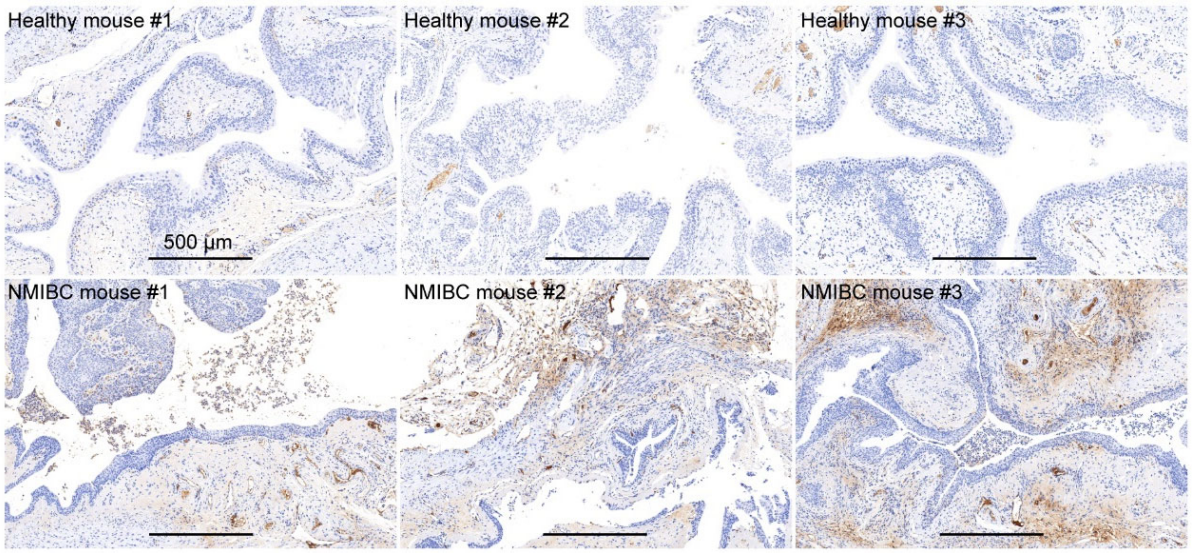


Supplementary Figure 8 | Tumour-targeting effect and efficient accumulation of NSs-RB-F/cRGD. a, Photographs (top) and corresponding H&E staining images (bottom) of dissected bladders from MNU-induced autochthonous bladder tumour mice (n = 5 mice). Black arrows: NMIBC regions. **b**, A representative photograph (top) and the corresponding H&E staining image (bottom) of the dissected bladder from a healthy mouse with only smooth and glossy serosa of the bladder. **c**, FTIR spectra of AEP, RB, cRGD-FITC, NSs, NSs-AEP, NSs-RB, and NSs-RB-F/cRGD. **d**,**e**, Fluorescence imaging of frozen slices (FITC channel, ex/em: 460-500/512-542 nm) (**d**) and quantitative FITC fluorescence signals with statistical analysis (**e**) of dissected bladders from a healthy mouse infused with NSs-RB-F/cRGD and NMIBC mice infused with NSs-RB-FITC and NSs-RB-F/cRGD (n = 3 mice). **f**,**g**, Fluorescence imaging of frozen slices (FITC channel, ex/em: 460-500/512-542 nm) (**f**) and quantitative FITC fluorescence signals (n = 3 mice) (**g**) in other two sections of the dissected bladder from the healthy mouse infused with NSs-RB-F/cRGD as control.

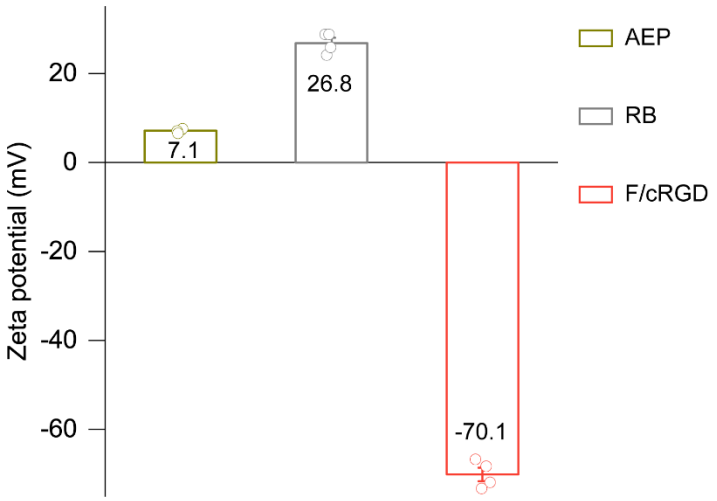
Data in **e** and **g** were presented as mean values +/- SEM. n = 6 independent experimental replicates. The *P* values in **e** were calculated by one-way ANOVA and multiple-comparison test.



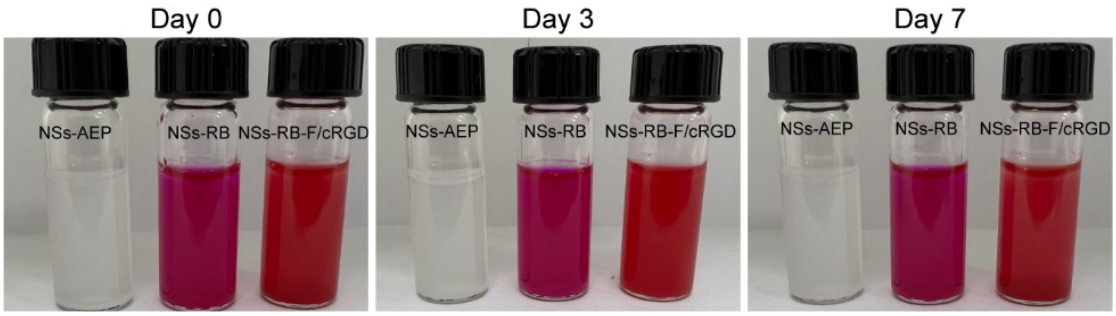
Supplementary Figure 9 | a, Absorption spectra of F/cRGD peptides at various concentrations. **b**, The linear fitting of F/cRGD peptides absorbance peak at 476 nm versus concentration. **c**, Absorption spectra of the supernatant after conjugation with F/cRGD peptides. Particularly, with the feeding mass amounts of NSs-RB and cRGD of 530 mg and 10 mg and the volume of supernatant to be 10 mL, the mass ratio of F/cRGD peptides onto the NS was determined to be 7.96:530 with the equation of (10-10*0.204):530.



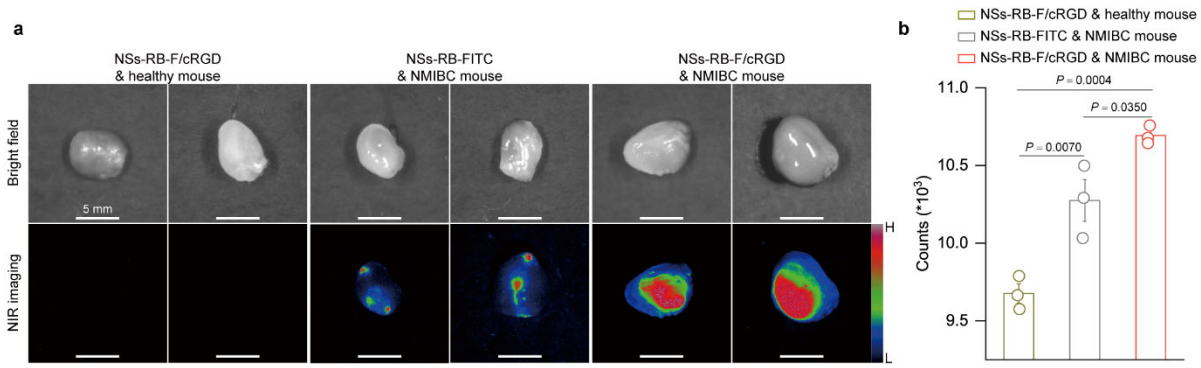
Supplementary Figure 10 | Expression of $\alpha_v\beta_3$ integrin in bladder tissues (n = 3 mice) NMIBC or healthy mice (Brown: $\alpha_v\beta_3$ Integrin-expressing cells; blue: nucleus)



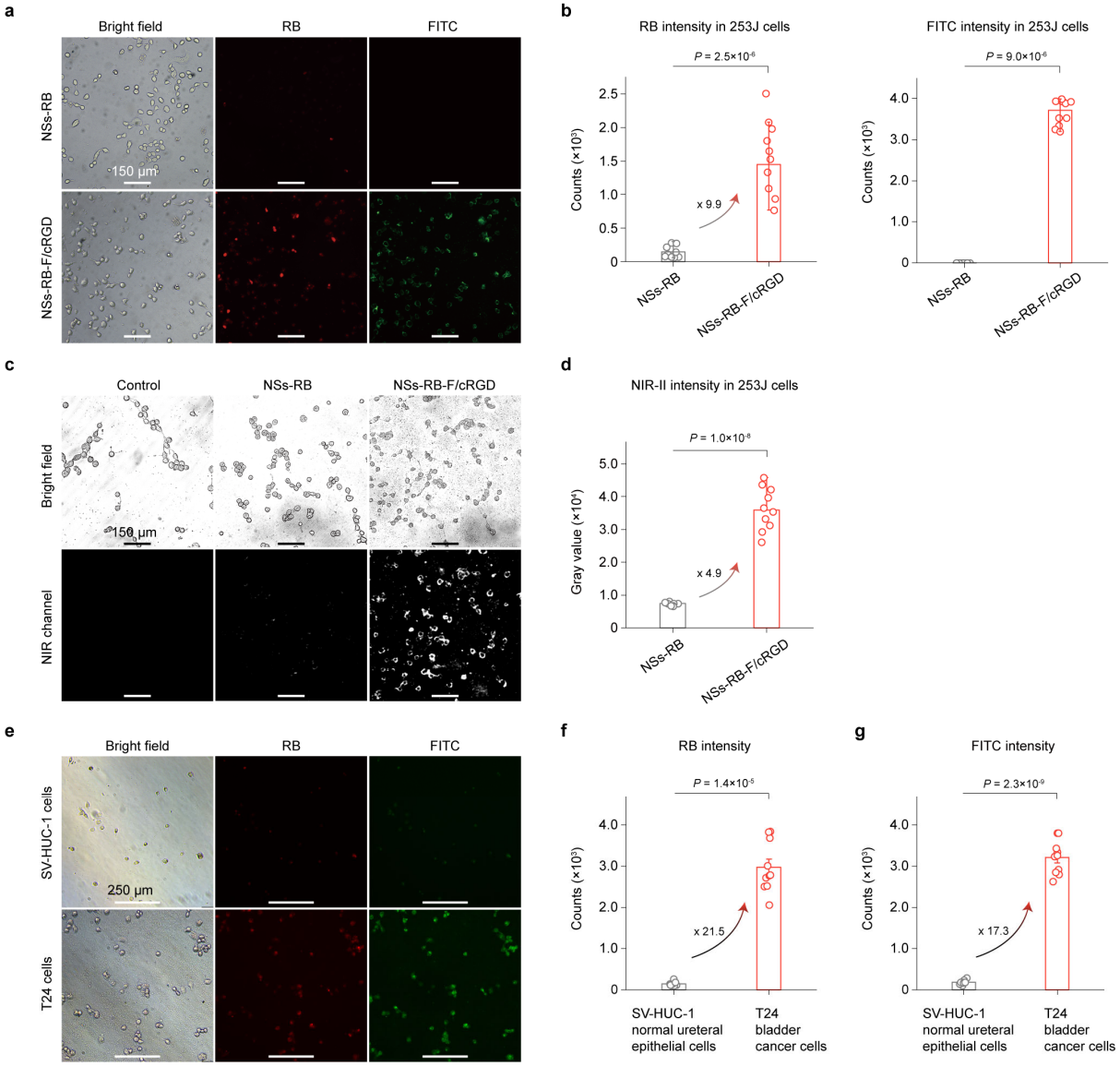
Supplementary Figure 11 | Zeta potentials (n = 4 independent experimental replicates) of AEP, RB, and cRGD-FITC. Data were presented as mean values +/- SEM.



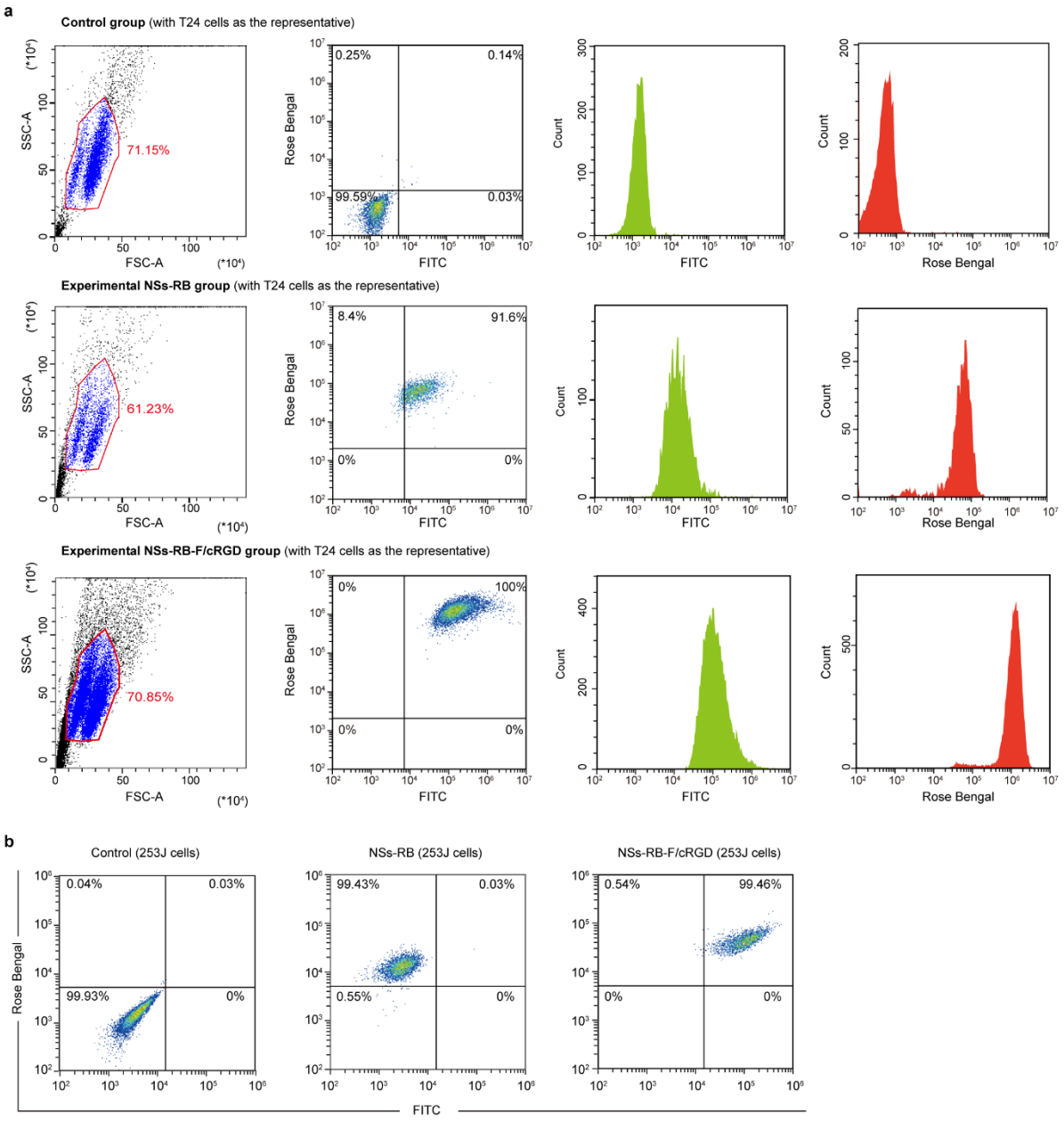
Supplementary Figure 12 | Stability of NSs-AEP, NSs-RB and NSs-RB-F/cRGD dispersed in PBS at different time.



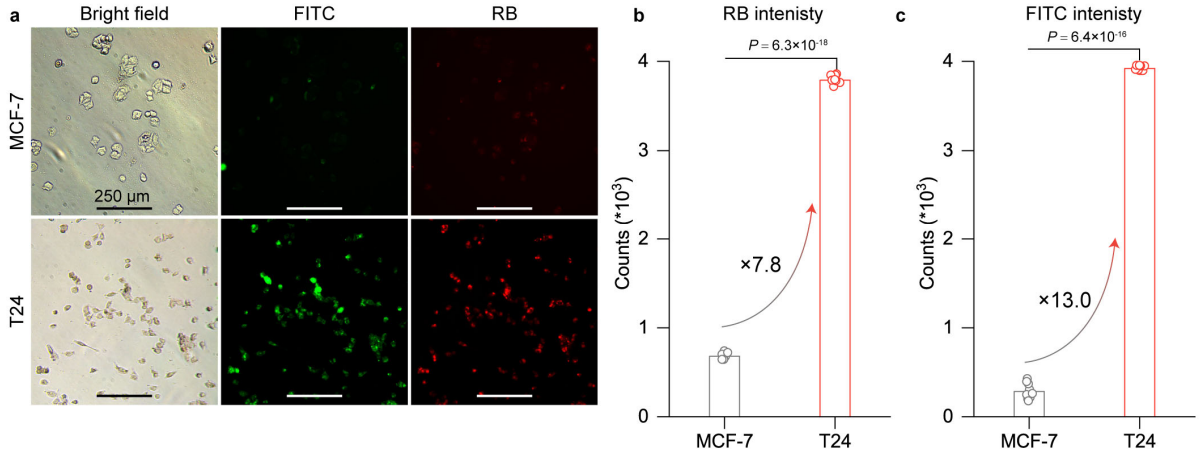
Supplementary Figure 13 | a, Ex vivo NIR-II fluorescence imaging (ex: 808 nm) of bladders dissected from the NSs-RB-F/cRGD-treated healthy mice and the NSs-RB-FITC-treated and NSs-RB-F/cRGD-treated NMIBC mice. **b**, Quantitative NIR-II fluorescence signals with statistical analysis in **a**. Data in **b** were presented as mean values +/- SEM. n = 3 mice. The *P* values in **b** were calculated by one-way ANOVA and multiple-comparison test.



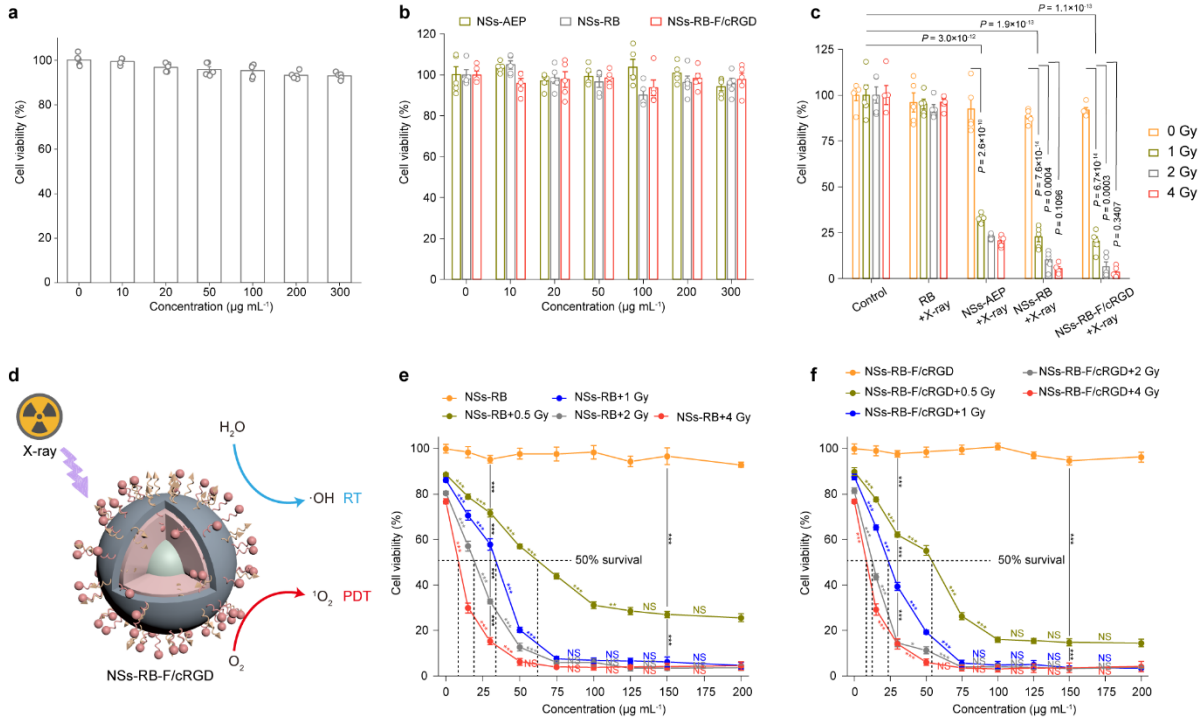
Supplementary Figure 14 | Accumulation of NSs-RB-F/cRGD in cancer cells and normal cells. **a**,**b**, Fluorescence imaging (**a**) and quantitative RB and FITC fluorescence intensities (**b**) in 253J cells incubated with NSs-RB and NSs-RB-F/cRGD (50 μg mL^{-1}). **c**,**d**, NIR-II fluorescence images (**c**) and quantitive signal intensity (**d**) in 253J cells with different treatments (50 μg mL^{-1}). **e**,**f**,**g**, Fluorescence imaging (**e**) and quantitative RB (**f**) and FITC fluorescence intensities (**g**) in normal ureteral epithelial cells of SV-HUC-1 and bladder cancer cells of T24 incubated with NSs-RB and NSs-RB-F/cRGD (50 μg mL^{-1}). Data in **b**, **d**, **f**, and **g** were presented as mean values +/- SEM. n = 10 independent experimental replicates. The *P* values in **b**, **d**, **f**, and **g** were calculated by paired two-sided Student's t-test.



Supplementary Figure 15 | Gating strategy of flow cytometry studies and related results. a, Representative gating strategy of flow cytometry studies in this study by taking control group and experimental groups of NSs-RB and NSs-RB-F/cRGD with T24 cells (data were shown in Fig. 2m) as representatives. For other flow cytometry analyses, similar gating strategies were adopted. **b**, Flow cytometry analysis of 253J cells after incubation with NSs-RB and NSs-RB-F/cRGD.

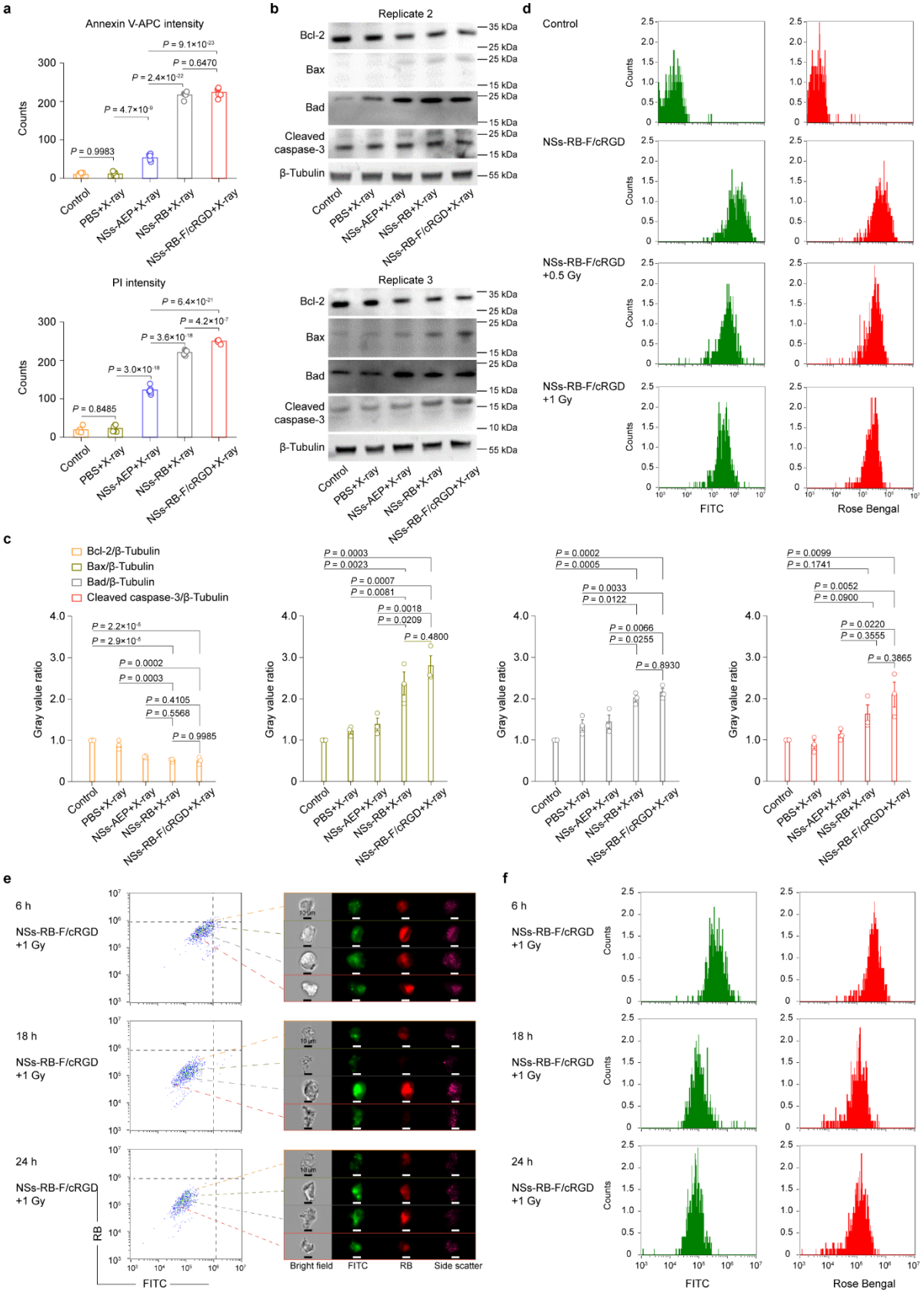


Supplementary Figure 16 | a,**b**,**c**, Fluorescence imaging (**a**) and quantitative RB (**b**) and FITC fluorescence intensities (**c**) in breast cancer cells of MCF-7 and bladder cancer cells of T24 incubated with NSs-RB-F/cRGD (50 μg mL^{-1}). Data in **b** and **c** were presented as mean values +/- SEM. n = 10 independent experimental replicates. The *P* values in **b** and **c** were calculated by paired two-sided Student's t-test.

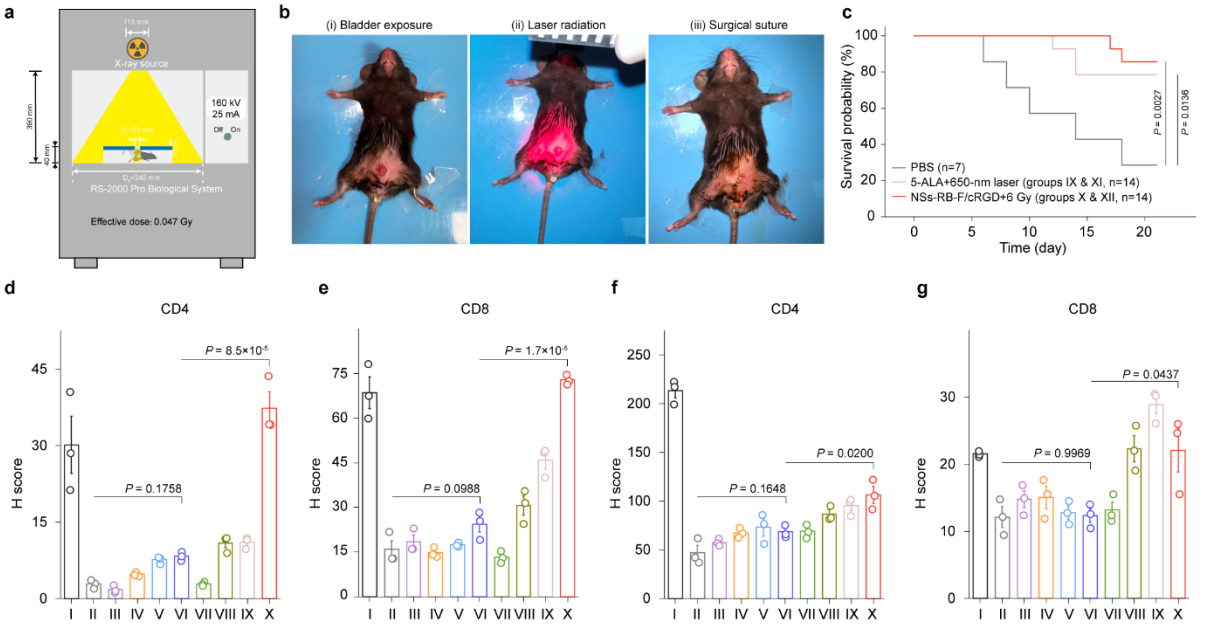


Supplementary Figure 17 | Cytotoxicity, radiosensitization assessment, and ROS generation of nanotransducers. a, Viabilities of SV-HUC-1 cells after incubation with NSs-RB-F/cRGD at different concentrations. **b**, Viabilities of 253J cells after incubation with NSs-AEP, NSs-RB, and NSs-RB-F/cRGD at different concentrations. **c**, Viabilities of 253J cells treated with PBS, RB, NSs-AEP, NSs-RB, and NSs-RB-F/cRGD with different X-ray doses. **d**, Mechanism of radiotherapy and photodynamic therapy based on NSs-RB-F/cRGD. **e**,**f**, Viabilities of T24 cells treated with NSs-RB (**e**) and NSs-RB-F/cRGD (**f**) with different concentrations at 0, 0.5, 1, 2, and 4 Gy. Data in **a**, **b**, **c**, **e** and **f** were presented as mean values +/- SEM. n = 5

independent experimental replicates. The *P* values in **c**, **e**, and **f** were calculated by one-way ANOVA and multiple-comparison test. **P* < 0.05, ***P* < 0.01, and ****P* < 0.0001. NS, no significant. The exact *P*-values were shown in Source Data.

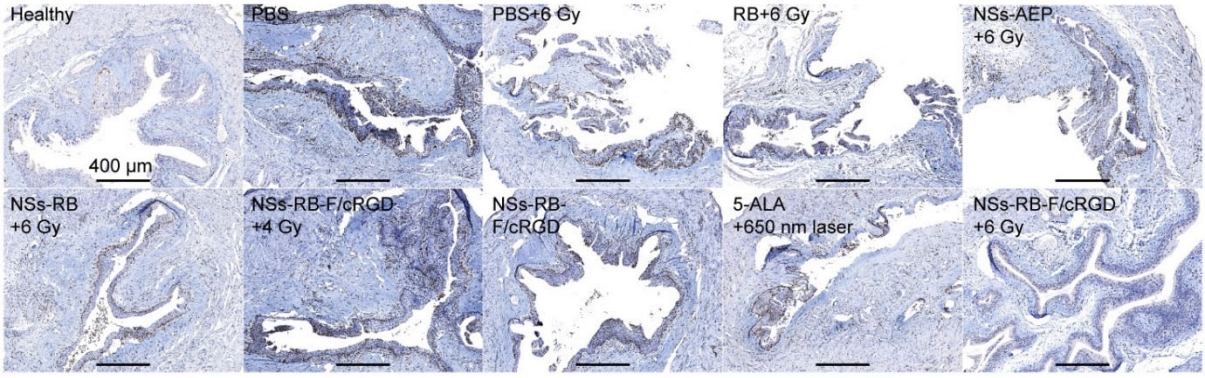


Supplementary Figure 18 | Apoptosis analysis and in vitro f-PDT assessment of nanotransducers. a, Quantification of Annexin V-APC/PI dual-staining assay of T24 cells with different treatments (n = 6 independent experimental replicates). **b**,**c**, Two additional biological replicates of Western blot analysis (**b**) and corresponding quantification and statistical analysis (n = 3 independent experimental replicates) (**c**) of protein expressions in T24 cells after receiving different treatments (50 μg mL^{-1}). **d**, Imaging flow cytometry histograms of T24 cells incubated for 12 h after different treatments (50 μg mL^{-1}). **e**,**f**, Imaging flow cytometry (n = 3 independent experimental replicates) (**e**) and corresponding histograms (**f**) of T24 cells incubated for 6, 18, and 24 h after different treatments (50 μg mL^{-1}). Data in **a** and **c** were presented as mean values +/- SEM. The *P* values in **a** and **c** were calculated by one-way ANOVA and multiple-comparison test.



Supplementary Figure 19 | Surgery-like laser-assisted PDT and survival rate estimation. a, X-Ray machine used for therapy given to mice and relevant geometrical parameters. **b**, Representative images of a bladder NMIBC mouse that reveal the protocol adopted in this study for surgery-like laser-assisted PDT (5-AIA+650-nm laser, 3 W). **c**, Survival probability of NMIBC mice receiving different treatments for 21 days. The two 5-ALA+laser groups (n = 7 mice, IX and XI) and the two NSs-RB-F/cRGD+6 Gy groups (n = 7 mice, X and XII) were combined to increase the sample number in each arm and increase statistical power for the comparison between laser-assisted PDT and single-f-PDT. Statistical analysis revealed that non-invasive single-f-PDT was more efficient compared to the invasive laser-assisted PDT. **d**,**e**, Quantification of CD4 (**d**) and CD8 cell proliferation (**e**) of bladders from healthy mice and NMIBC mice of all groups (n = 3 mice). **f**,**g**, Quantification of CD4 (**f**) and CD8 cell proliferation (**g**) of spleens from healthy mice and NMIBC mice of all groups (n = 3 mice). Data analysis in **c** was performed using a log-rank (Mantel-Cox) test and post-Bonferroni correction (α=0.05/n (n = 2). Data in **d-g** were presented as mean values +/- SEM. The *P* values

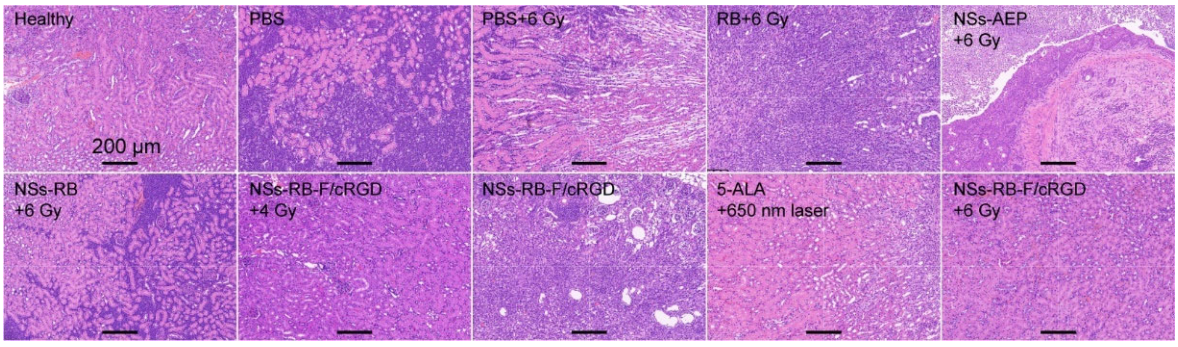
in **d-g** were calculated by one-way ANOVA and multiple-comparison test.



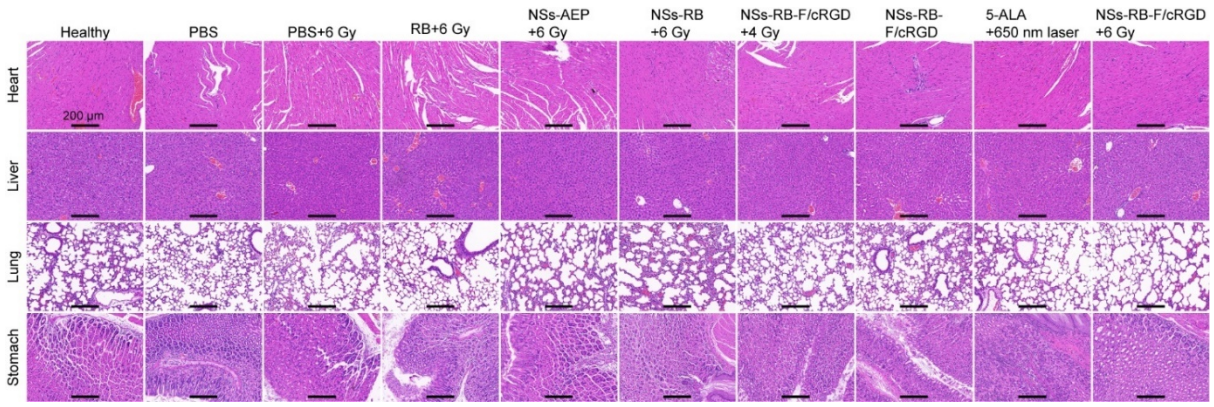
Supplementary Figure 20 | Ki-67 staining of bladders obtained from each treatment groups (n = 7 mice).



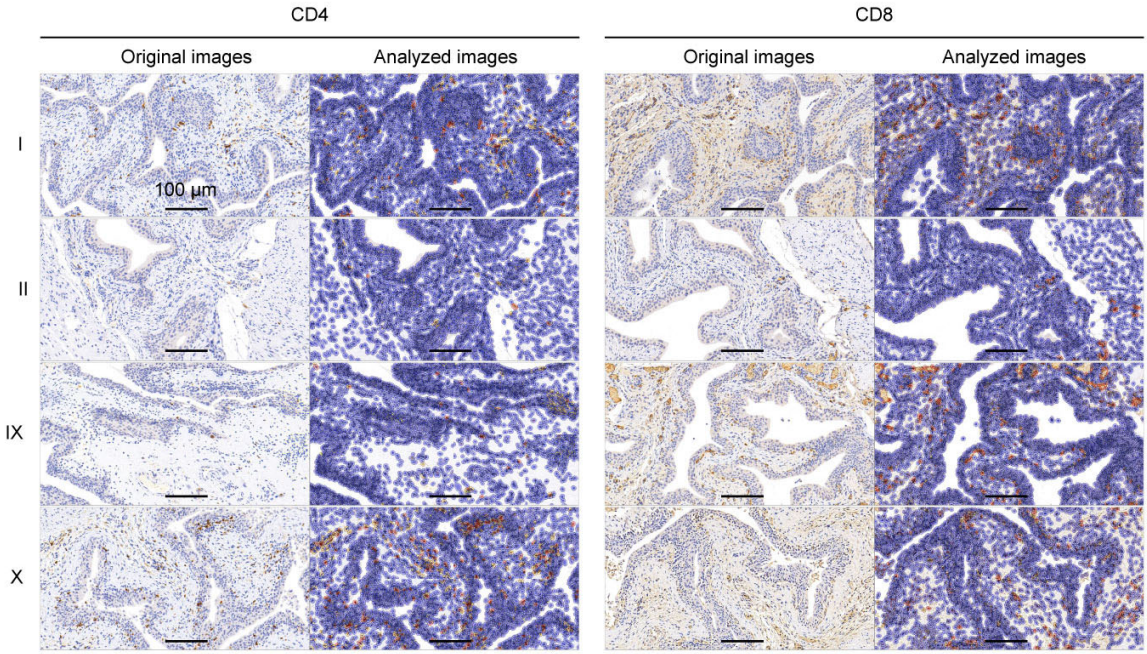
Supplementary Figure 21 | Representative images of kidneys dissected from different treatment groups at day 21 (n = 7 mice).



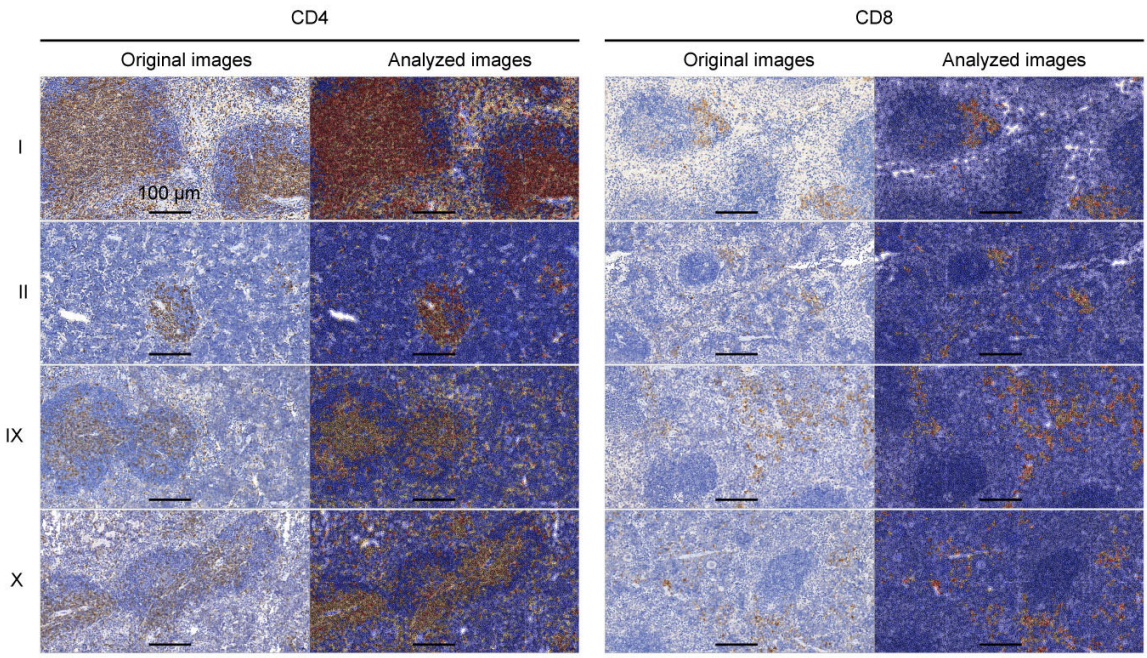
Supplementary Figure 22 | Representative H&E staining images of kidneys dissected from different treatment groups at day 21 (n = 7 mice).



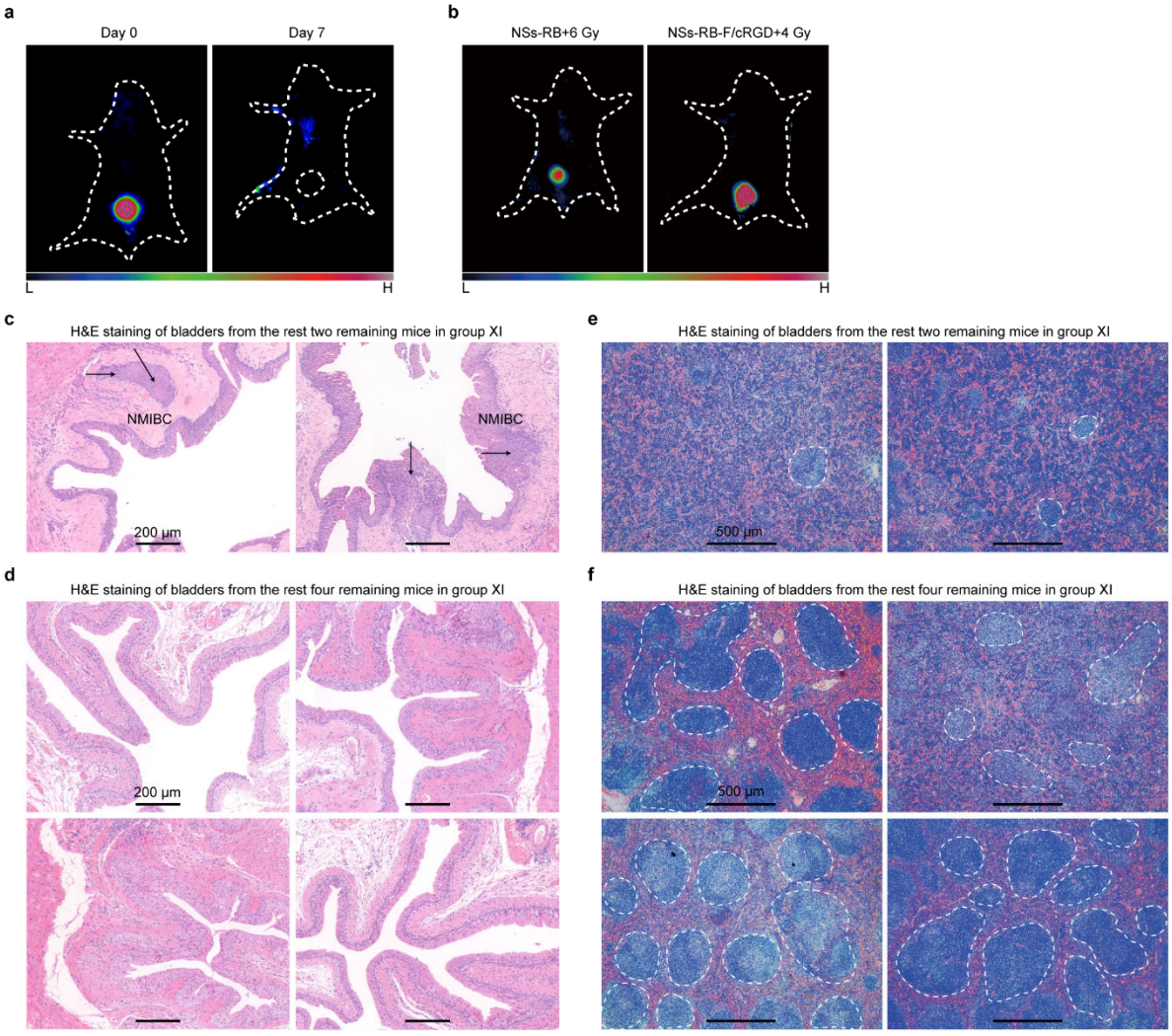
Supplementary Figure 23 | H&E staining images of major organs (heart, liver, lung and stomach) from NMIBC mice receiving different treatments at Day 21, showing no abnormal or metastasis signature (n = 7 mice).



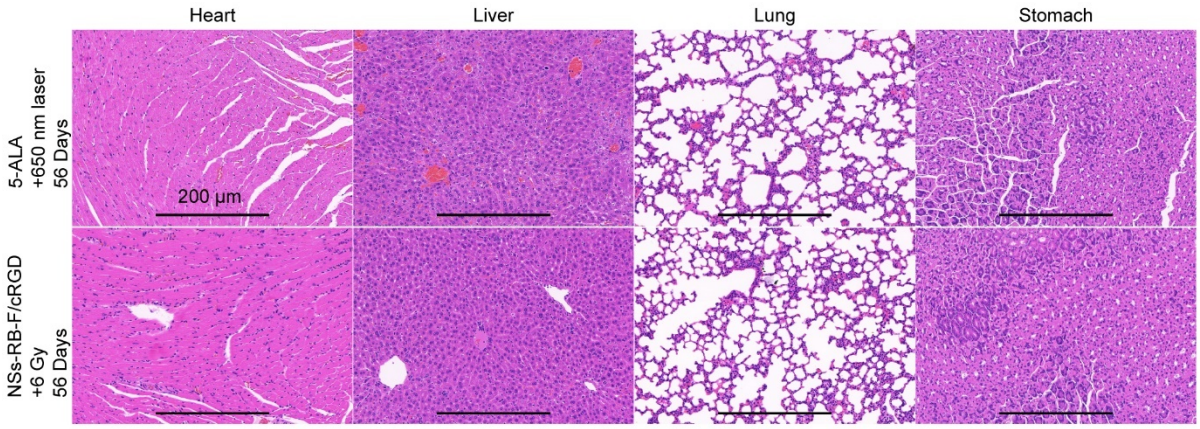
Supplementary Figure 24 | Representative original immunohistochemistry images (n = 3 mice) of the bladders dissected from different treatment groups at day 21 and analyzed images by using the widely accepted German semi-quantitative scoring system (I: Blank; II: PBS; IX: 5-ALA+650 nm laser; X: NSs-RB-F/cRGD+6 Gy). More details can be found in Methods.



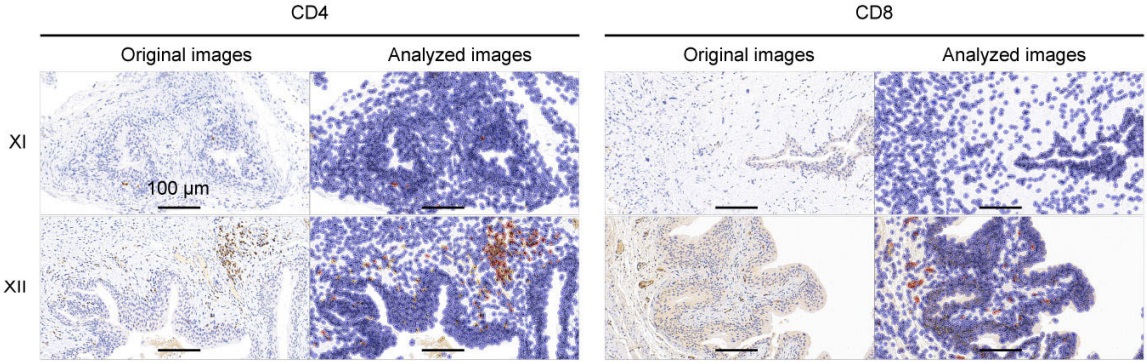
Supplementary Figure 25 | Representative original immunohistochemistry images (n = 3 mice) of the spleens dissected from different treatment groups at day 21 and analyzed images by using the widely accepted German semi-quantitative scoring system (I: Blank; II: PBS; IX: 5-ALA+650 nm laser; X: NSs-RB-F/cRGD+6 Gy). More details can be found in Methods.



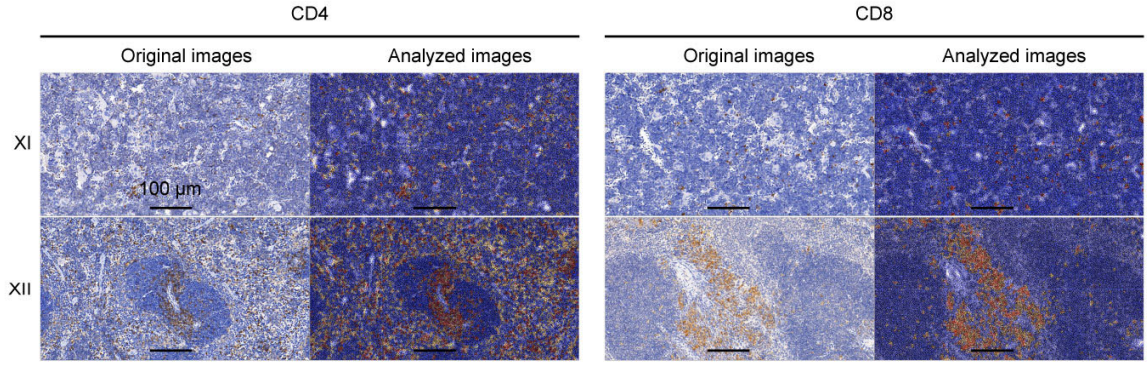
Supplementary Figure 26 | Data for post-operative monitoring and recurrence inhibition by single-f-PDT. a, NIR-II fluorescence images of NMIBC mice taken at days 0 and 7 after intravesical infusion of 100 μL of 10 mg mL^{-1} NSs-RB-F/cRGD for 1 h, which indicated that NSs-RB-F/cRGD was excreted within 7 days. **b**, NIR-II fluorescence images taken at day 14 with slightly increased signal intensities of one mouse of each group of NSs-RB+6 Gy and NSs-RB-F/cRGD+4 Gy, which revealed the sensitivity and convenience of non-invasive real-time in vivo imaging for tumour development monitoring. **c**,**d**, H&E staining images of bladders dissected from the rest two mice in group XI (**c**) and the rest four mice in group X (**d**). Black arrows show the existence of recurrent tumour regions. **e**,**f**, H&E staining images of spleens dissected from the rest two mice in group XI (**e**) and the rest four mice in group X (**f**). White boxes show intact splenic regions. n = 7 mice.



Supplementary Figure 27 | H&E staining images of major organs (heart, liver, lung and stomachs) from NMIBC mice receiving different treatments at Day 56, showing no abnormal or metastasis signature. n = 7 mice)

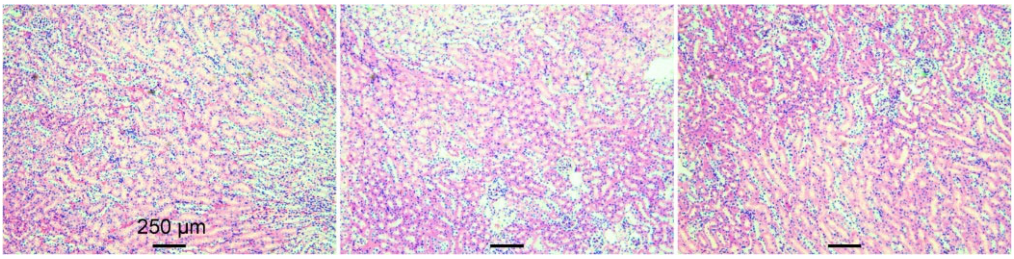


Supplementary Figure 28 | Representative original immunohistochemistry images (n = 3 mice) of the bladders dissected from different treatment groups at day 56 and analyzed images by using the widely accepted German semi-quantitative scoring system (XI: 5-ALA, 650 nm laser; XII: NSs-RB-F/cRGD+6 Gy). More details can be found in Methods.

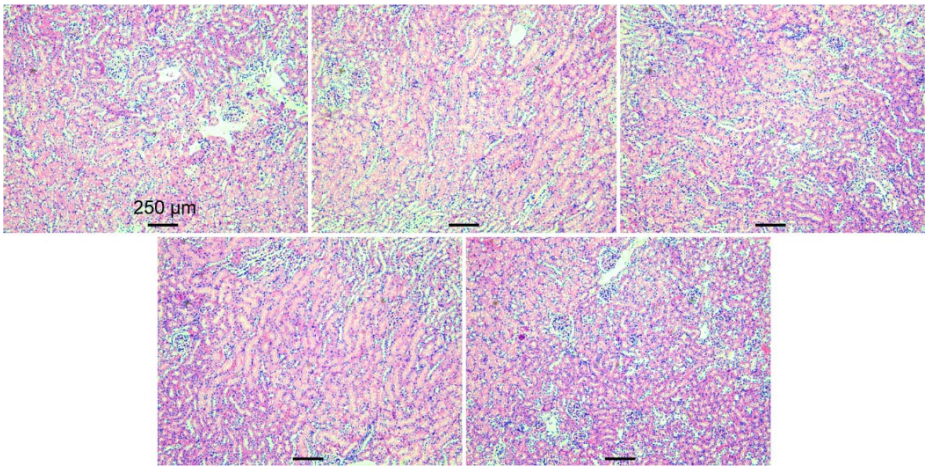


Supplementary Figure 29 | Representative original immunohistochemistry images (n = 3 mice) of the spleens dissected from different treatment groups at day 56 and

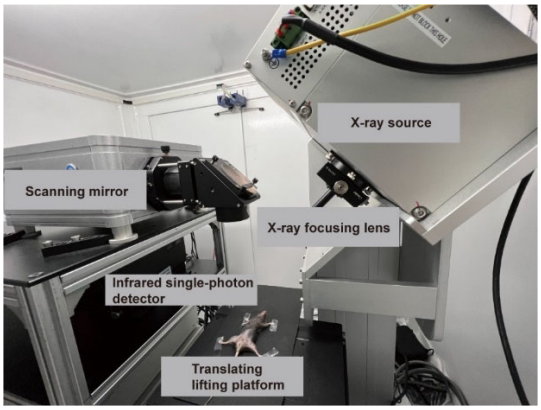
analyzed images by using the widely accepted German semi-quantitative scoring system (XI: 5-ALA, 650 nm laser; XII: NSs-RB-F/cRGD+6 Gy). More details can be found in Methods.



Supplementary Figure 30 | H&E staining images of kidneys dissected from the three remaining mice receiving treatment of 5-ALA+laser (n = 7 mice. XI group: 5-ALA+650 nm laser, 56 Day).

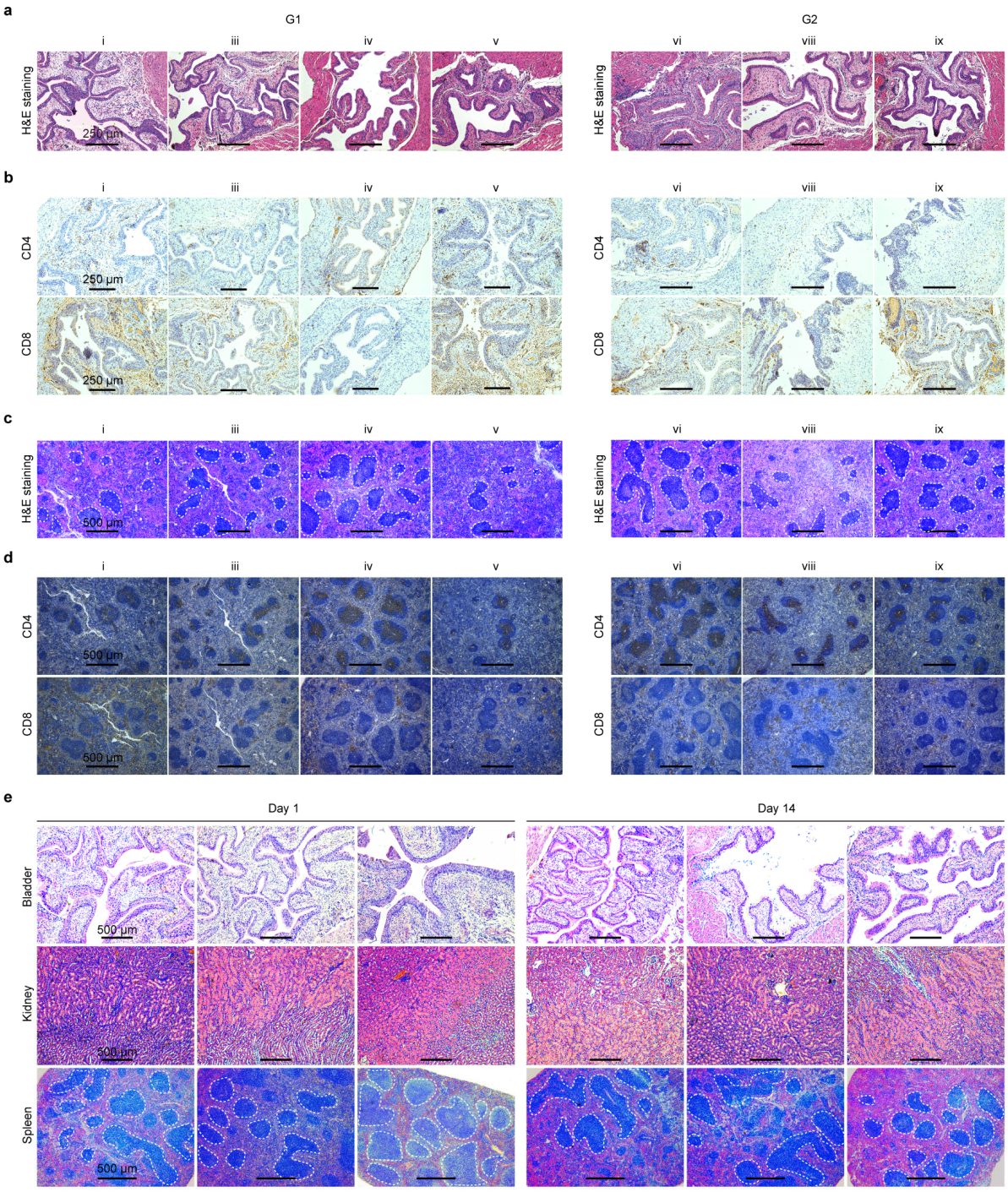


Supplementary Figure 31 | H&E staining of kidneys dissected from the five remaining mice receiving treatment of NSs-RB-F/cRGD+6 Gy (n = 7 mice. XII group: NSs-RB-F/cRGD+6 Gy, 56 Day).

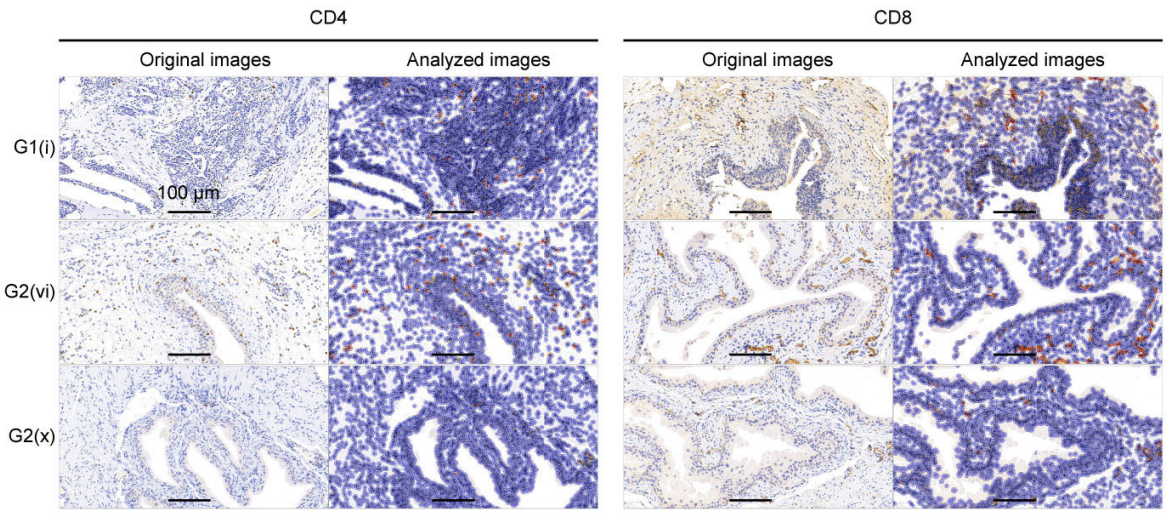


Supplementary Figure 32 | A photograph of our lab-made system with the main components of the X-ray source, 808-nm laser, detector, and platform components

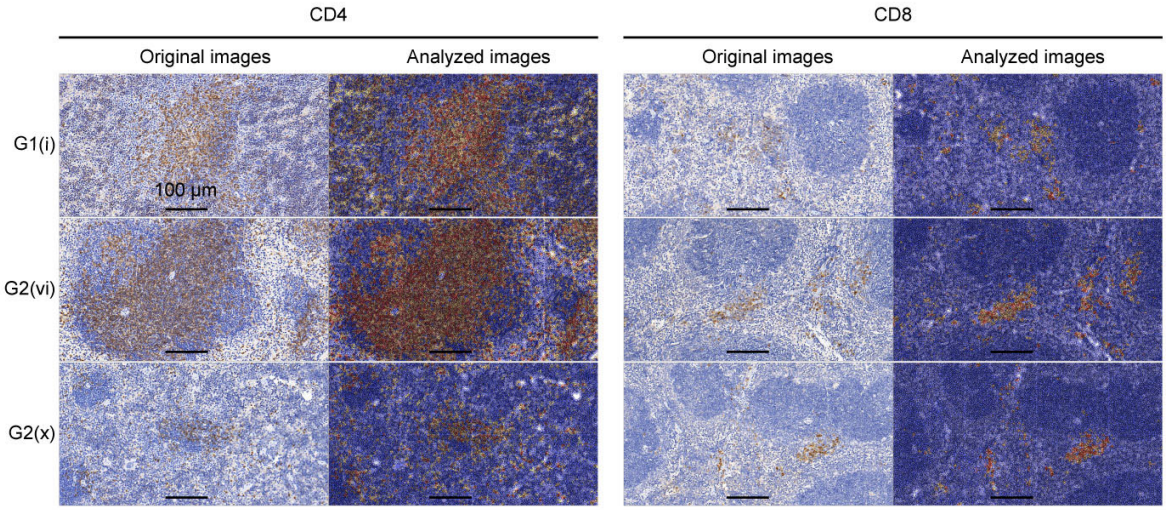
outlined.



Supplementary Figure 33 | Data for customized f-PDT and safety estimation. a,**b**, H&E staining images (**a**) and immunohistochemistry analysis (**b**) of bladders dissected from the rest mice in G1 and G2 (n = 5 mice). **c**,**d**, H&E staining images (**a**) and immunohistochemistry analysis (**b**) of spleens dissected from the rest mice in G1 and G2. **e**, H&E staining images of bladder, kidneys, and spleen from healthy mice taken at day 1 and 14 after being treated with NSs-RB-F/cRGD (n = 4 mice).



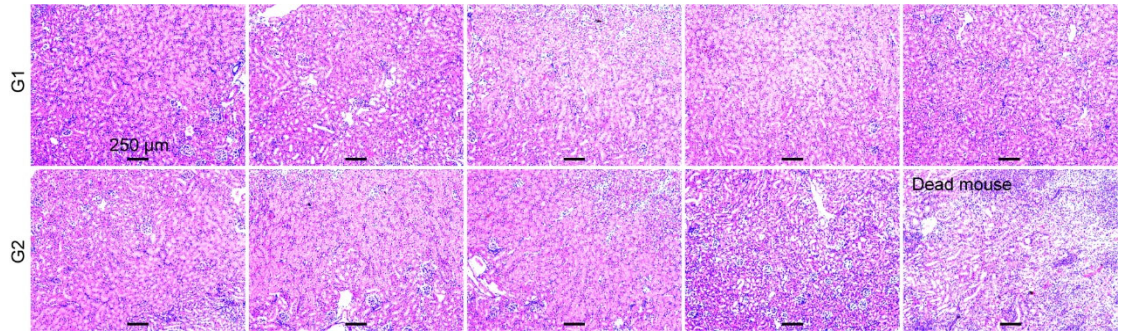
Supplementary Figure 34 | Representative original immunohistochemistry images (n = 5 mice) of the bladders dissected from the survived mice in G1 and G2 at day 56 and from G2(x) at day 31 by using the widely accepted German semi-quantitative scoring system. More details can be found in Methods.



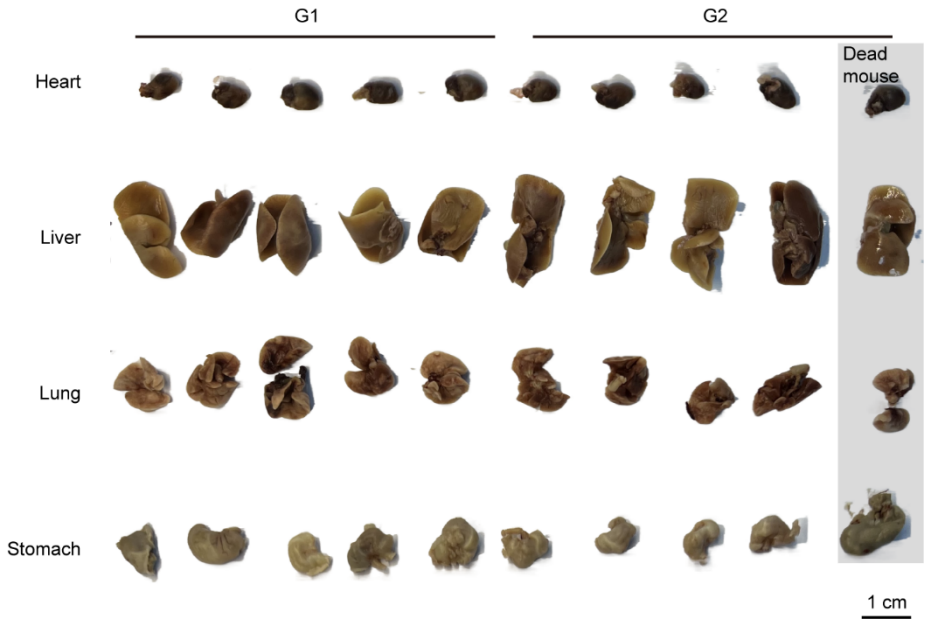
Supplementary Figure 35 | Representative original immunohistochemistry images (n = 5 mice) of the spleens dissected from the survived mice in G1 and G2 at day 56 and from G2(x) at day 31 by using the widely accepted German semi-quantitative scoring system. More details can be found in Methods.



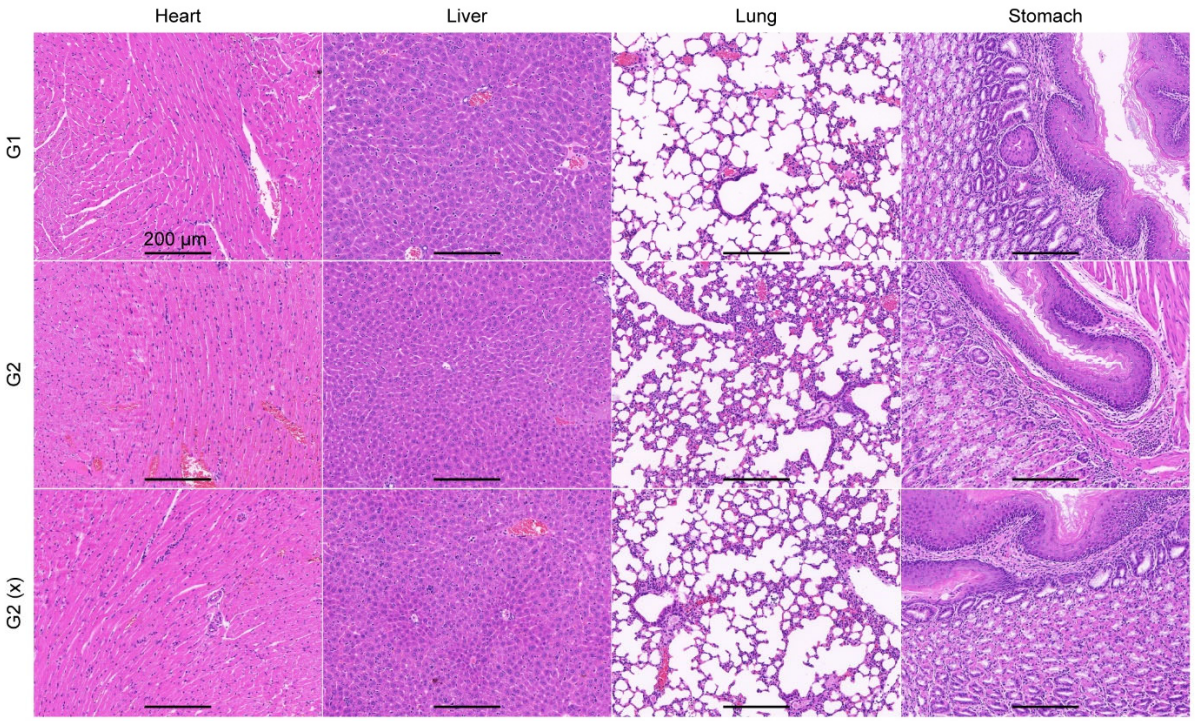
Supplementary Figure 36 | Photographs of kidneys dissected from the nine remaining mice taken at day 56 and that of the mouse died at day 31 (n = 5 mice).



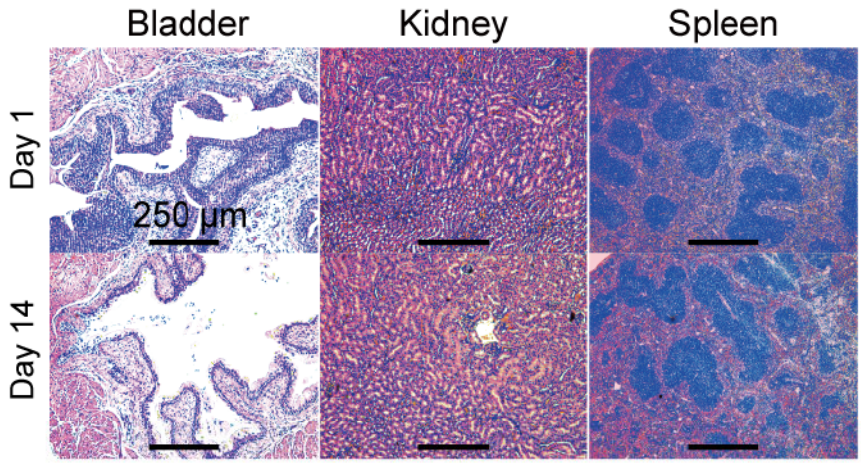
Supplementary Figure 37 | H&E staining of kidneys dissected from the nine remaining mice at day 56 and the mouse died at day 31 (n = 5 mice).



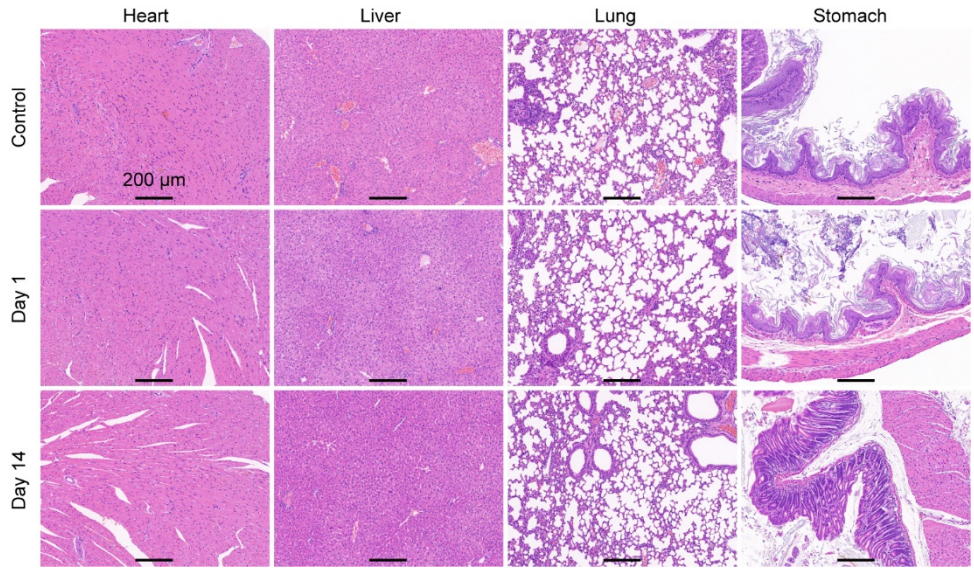
Supplementary Figure 38 | Photographs of organs (heart, liver, lung, and stomach) dissected from the nine remaining mice at day 56 and the mouse died at day 31 (n = 5 mice).



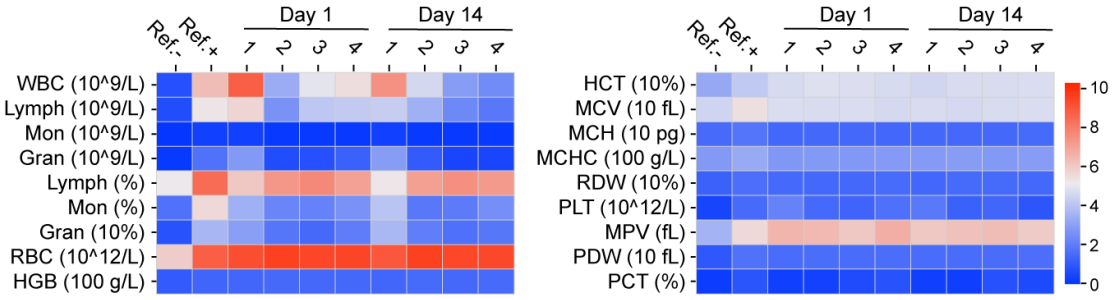
Supplementary Figure 39 | H&E staining images of major organs (heart, liver, lung and stomachs) dissected from mice in G1 and G2 at day 56 and G2(x) at day 31, showing no abnormal or metastasis signature (n = 5 mice).



Supplementary Figure 40 | Representative H&E staining images of healthy mice that received pre-intravesical instillation of NSs-RB-F/cRGD as used for treatment (n = 4 mice).



Supplementary Figure 41 | H&E staining of major organs (heart, liver, lung, and stomach) of healthy mice with different exposure periods to NSs-RB-F/cRGD (n = 4 mice).



Supplementary Figure 42 | Blood routine of healthy mice that received pre-intravesical instillation of NSs-RB-F/cRGD as used for treatment (n = 4 mice).

Supplementary Tables

Supplementary Table 1 | Calculated parameter values and fitted formula based on the radiosensitization activity of PBS and NSs-AEP in T24 cells.

	D_0	N	SER50	fitted formula
PBS+X-ray	7.115	1.081	5.315	$SF=1-(1-e^{-0.141D})^{1.081}$
NSs-AEP+X-ray	5.108	0.501	1.471	$SF=1-(1-e^{-0.196D})^{0.501}$

Supplementary Table 2 | Urine routine test of mice evaluated at day 1 and day 14 after intravesical instillation with NSs-RB-F/cRGD (n = 4 mice).

Para.	Unit	Day 1				Day 14				*Ref.*
		1	2	3	4	1	2	3	4	
WBC	CELL/uL	0	0	0	0	0	0	0	0	0-15
KET	mmol/L	0	0	0.5	0.5	0	0	0	1.5	0-0.5
NIT	/	-	-	-	-	-	-	-	-	-
URO	umol/L	*Norm.*	*Norm.*	*Norm.*	*Norm.*	*Norm.*	*Norm.*	*Norm.*	*Norm.*	*Norm.*
BIL	umol/L	0	0	0	0	0	0	0	0	0
PRO	g/L	0.15	0.15	0	0.3	0.3	0.15	0.15	0.15	0-0.15
GLU	mmol/L	0	0	0	0	0	0	0	0	0-2.8
SG	/	1.005	1.01	1.025	1.01	1.01	1.01	1.01	1.015	1.005-1.030
PH	/	7.5	7.5	6.5	7.5	8	7.5	8	6	5.0-9.0
BLD	CELL/uL	0	0	0	0	0	0	0	0	0
CR	mmol/L	≤0.9	≤0.9	≤0.9	≤0.9	≤0.9	≤0.9	≤0.9	≤0.9	≤0.9
Ca	mmol/L	≤1.0	≤1.0	≤1.0	≤1.0	≤1.0	≤1.0	≤1.0	≤1.0	≤1.0
MA	mg/L	≤10	≤10	≤10	≤10	≤10	≤10	≤10	≤10	≤10

Supplementary Table 3 | Blood routine test of mice evaluated at day 1 and day 14 after intravesical instillation with NSs-RB-F/cRGD (n = 4 mice).

Parameters	Day 1				Day 14				*Ref.*
	1	2	3	4	5	6	7	8	
WBC (10^9/L)	9.4	3.6	5.3	5.9	8	4.9	3.1	2.6	0.8-6.8
Lymph (10^9/L)	6.1	2.8	4.4	4.5	4.6	3.7	2.5	2	0.7-5.7
Mon (10^9/L)	0.3	0.1	0.1	0.1	0.3	0.1	0.1	0.1	0-0.3
Gran (10^9/L)	3	0.7	0.8	1.3	3.1	1.1	0.5	0.5	0.1-1.8
Lymph (10%)	6.47	7.83	8.21	7.56	5.66	7.62	8.02	7.76	5.58-9.06
Mon (%)	3.7	2.4	2.3	2.8	4.3	2	2.1	2.7	1.8-6.0
Gran (10%)	3.16	1.93	1.56	2.16	3.91	2.18	1.77	1.97	0.86-3.89
RBC (10^12/L)	9.9	10.26	10.07	10.11	9.61	10.23	10.05	10.02	6.36-9.42
HGB (100 g/L)	1.47	1.56	1.53	1.52	1.47	1.57	1.53	1.58	1.1-1.43
HCT (10%)	5	5.18	5.11	5	4.84	5.04	5.05	5.08	2.46-4.46
MCV (10 fL)	5.06	5.05	5.08	4.95	5.04	4.93	5.03	5.07	4.82-5.83
MCH (10 pg)	1.48	1.52	1.51	1.5	1.52	1.53	1.52	1.57	1.58-1.9
MCHC (100 g/L)	2.94	3.01	2.99	3.04	3.03	3.11	3.02	3.11	3.02-3.53
RDW (10%)	1.54	1.51	1.51	1.6	1.48	1.57	1.57	1.51	1.3-1.7

PLT (10^12/L)	2.295	1.55	1.412	1.769	2.041	1.306	1.461	0.941	0.45-1.59
MPV (fL)	7	6.9	6.5	7.2	6.5	6.7	6.8	6.4	3.8-6.0
PDW (10 fL)	1.65	1.66	1.63	1.66	1.63	1.64	1.63	1.7	1.0-1.8
PCT (%)	0.282	0.348	0.65	0.851	0.284	0.249	0.819	0.602	0.2-0.9